fractal and fractional

MDPI

Article

Fractional-Order Event-Triggered Control of HIV on Heterogeneous Networks: Robust Contraction and Spectral Targeting

Tingting Dai [1,2], Haiying Wang [1,*], Yuan Zhou [1], Qingyuan Wang [1] and Shaohui Wang [3]

[1] School of Science, China University of Geosciences (Beijing), Beijing 100083, China; daitingting@ztu.edu.cn (T.D.); 2019240015@email.cugb.edu.cn (Y.Z.); 18031243061@163.com (Q.W.)
[2] School of Mathematics and Statistics, Zhaotong University, Zhaotong 657000, China
[3] Department of Mathematics, Louisiana Christian University, Pineville, LA 71359, USA; shaohui.wang@lcuniversity.edu
* Correspondence: whycht@cugb.edu.cn

Abstract

We analyze a campaign-renewed Caputo model of HIV transmission on heterogeneous contact networks, with risk-triggered screening and antiretroviral-treatment linkage. The model has a spectral next-generation threshold and an explicit positive matrix Mittag–Leffler jump–flow operator. Positivity, global extinction under a positive linear resolvent comparison, and conditional robust hybrid-contraction theorems are established without assuming that the nonlinear infected–treated subsystem is cooperative. A common weighted norm and watchdog-bounded intervention intervals are required; these assertions do not apply unmodified to a fixed-history Caputo system. An independent reconstruction of the complete 80-dimensional cycle matrix gives spectral radius 1.0688 for the stated nominal baseline ($\alpha = 0.85$, one-year cycle), correcting an earlier noncontractive setting that had been described as stabilizing. A separate six-mode intervention family admits a common weighted-norm bound below 0.9981. Newly executed nonlinear 20-year experiments, including mandatory watchdog events, report actual campaign counts, ART transfers and burden under single-factor and nominal-budget-matched comparisons; a periodic strategy can outperform risk-triggered intervention at the same total nominal pulse budget. Three seeded 100-graph synthetic ensembles clarify structural variability but do not certify arbitrary switching. Beijing surveillance counts from 2005 to 2020 are independently redrawn with one missing AIDS observation marked explicitly; these data do not empirically identify the fractional order, contact network or controller.

Keywords: fractional-order HIV dynamics; heterogeneous contact networks; event-triggered control; risk-targeted intervention; Caputo derivative; Mittag–Leffler stability; spectral threshold

MSC: 26A33; 34A08; 34D20; 92D30; 93D20; 05C82

Check for updates

Academic Editor: Da-Yan Liu

Received: 27 September 2026
Revised: 22 October 2026
Accepted: 24 October 2026
Published: 30 October 2026

Copyright: © 2026 by the authors. Licensee MDPI, Basel, Switzerland. This article is an open access article distributed under the terms and conditions of the Creative Commons Attribution (CC BY) license.

1. Introduction

Network heterogeneity is one of the main structural mechanisms that separates population-average epidemic models from contact-driven transmission processes. Degree variability, assortative mixing, and the position of infected individuals within a contact graph can change invasion thresholds and the marginal value of targeted intervention [1–4]. Classical network immunization studies likewise show that structural information can be used

to concentrate limited preventive resources [5–8]. In HIV control, however, topology alone does not determine the intervention problem: antiretroviral treatment and pre-exposure prophylaxis can substantially reduce transmission risk [9–11], so an analytically useful framework should decide not only where intervention effort is most valuable, but also when a campaign should be activated. This motivates a control architecture in which network structure determines allocation while a state-dependent epidemic burden determines timing.

The second issue is temporal memory, and this motivates exploring a fractional formulation as one possible phenomenological description of temporal dependence, rather than claiming that a particular fractional order is empirically necessary. Standard integer-order epidemic models are Markovian once the state has been specified, whereas Caputo systems retain a nonlocal power-law history through their convolution kernel [12–14]. The associated stability theory is governed by fractional sector conditions and Mittag–Leffler decay rather than by an ordinary exponential semigroup [15,16]. Fractional HIV models have therefore been used to represent hereditary infection and treatment effects under several operators [17–19]. For the present control problem, this distinction is operational: between campaigns the integer-order linearized flow is $\exp(A\Delta)$, while the fractional flow is $E_\alpha(A\Delta^\alpha)$. Consequently, α changes post-campaign relaxation, trigger-crossing times, and the gain of the complete intervention cycle even when the algebraic invasion threshold is unchanged. The memory order therefore enters the specified controller model, but this does not identify α from surveillance data or exclude alternative integer-order models with additional latent states.

A third line of work concerns event-triggered and impulsive control. Event-triggered feedback was developed to reduce unnecessary communication or actuation while preserving stability [20,21], and event-triggered impulsive control has been extended to nonlinear and delayed systems with explicit Zeno-exclusion conditions [22]. Hybrid-system theory provides the general language for combining continuous flows with state-dependent jumps [23], while recent impulsive-control studies have refined Lyapunov and event-triggered stability tools for stochastic, delayed, and networked systems [24–27]. In parallel, Fractal and Fractional has recently published event-triggered and distributed control designs for fractional-order networked systems [28–31]. These studies establish the relevance of fractional event-triggered control, but they do not resolve the specific combination considered here: a heterogeneous HIV contact network, a risk-triggered screening-to-treatment jump, a fractional jump–flow stability operator, and a topology-aware finite-budget targeting rule derived from that operator. Recent journal-specific examples sharpen this distinction: Li et al. [19] analyze a fractional HIV/AIDS model with drug control but without an event-triggered contact-network control layer, whereas Li [28] develops data-driven event-triggered control for general fractional-order networked systems but not for epidemic transmission or cycle-level topology-aware allocation. More directly, Liu et al. [32] proposed a fractional-order epidemic model on a weighted network with time delay and an infection-rate-threshold event-triggered impulsive controller, including an explicit Zeno-exclusion analysis. This is the closest combined epidemic/event-triggered baseline found in our literature review. Its contribution establishes that fractional epidemic network dynamics and event-triggered impulses can be coupled; the present study therefore does not claim novelty for that combination alone. Instead, the unresolved issue is whether an HIV-specific heterogeneous network can be controlled through a cycle-level Mittag–Leffler operator that supports uniform robust contraction and simultaneously induces a finite-budget Perron targeting rule. To our knowledge, the surveyed literature does not provide such a single HIV network framework.

The closest epidemic-network baseline is Liu et al. [33], who formulated a fractional-order SIR model on a two-layer weighted network, analyzed disease-free stability, and pro-

posed targeted immunity according to network-related risk. Their study demonstrates that fractional memory and weighted network structure can be combined effectively in epidemic modeling. Its intervention layer is nevertheless essentially structural and static: the target set is prescribed from network or demographic information, and the main stability question concerns the epidemic equilibrium. In contrast, the present work makes intervention timing endogenous. A degree-weighted HIV burden is monitored continuously, a screening-to-ART jump is activated only when the burden reaches a risk threshold, and the control objective is evaluated through the complete fractional event-to-event operator rather than through a static network-weight criterion alone.

A complementary control-theoretic benchmark is the event-triggered impulsive stabilization framework for fractional-order switched systems developed by Gokul et al. [34]. That work addresses Zeno avoidance, finite-time stability, and finite-time contractive stability under a mode-dependent event-triggered mechanism. The present problem differs in both structure and objective. We do not switch among abstract subsystems; the fractional flow is generated by a heterogeneous HIV transmission operator, the jump represents rapid testing and treatment linkage, and the design target is the dominant gain of an epidemic flow–jump cycle. This leads to two control objects that are absent from the static epidemic setting: a matrix Mittag–Leffler jump–flow operator and a Perron spectral-sensitivity allocation rule that couples fractional memory, network topology, intervention timing, and finite-resource targeting.

The unresolved gap is therefore not whether fractional memory, event triggering, or network targeting can be used separately, but whether they can be coupled through a single stability object that remains analytically interpretable under uncertainty and yields a concrete allocation rule. The present study addresses that gap by making the fractional event-to-event operator the common object linking stability analysis, trigger timing, and network targeting.

The main technical difficulty is that fractional dynamics and event-triggered impulsive control cannot be combined by a formal replacement of an integer derivative. A Caputo system does not possess the ordinary semigroup property, and the lower terminal of the memory kernel must be specified at intervention times. We therefore adopt a campaign-renewed Caputo convention in which each intervention time becomes the lower terminal of the next post-campaign memory interval. This convention is used as an intervention-cycle modeling device: each campaign initiates a new observation-and-linkage episode and thereby produces the analyzable cycle operator $J(U)E_{\alpha}(A\Delta^{\alpha})$. It is not interpreted as a claim that biological history is physically erased. The manuscript also reports a newly reconstructed finite-horizon numerical comparison of the renewed-memory model and an explicitly defined fixed-history impulsive Volterra convention. This comparison is not a proof of full-history stability. In the limit $\alpha \to 1$, the proposed operator converges to the classical jump–flow operator, providing an exact integer-order benchmark.

Accordingly, the contribution is not a fractionalized HIV model with an appended control term, but a fractional network-control framework built around the interaction of memory, event timing, and topology. Specifically, the paper (i) formulates a campaign-renewed Caputo HIV model on heterogeneous contact networks; (ii) co-designs a risk trigger and a degree-dependent screening-to-treatment jump; (iii) derives the network spectral invasion threshold and establishes positivity, invariance, and Mittag–Leffler disease-free stability; (iv) develops a fractional jump–flow theory giving non-Zeno triggering, uniform cycle contraction, nonlinear eradication, and robust stability under uncertainty in memory order, topology, parameters, and timing; (v) derives a Perron spectral-sensitivity score and a budget-constrained first-order allocation rule for correlated networks; and (vi) organizes the numerical study so that each major analytical claim is paired with a cor-

responding diagnostic, including an equal-effort periodic-control ablation and the original 100-realization synthetic-network illustrations alongside independently audited complete-cycle computations; the ensemble draws do not provide a common-norm certificate. Relative to Liu et al. [33], the increment is dynamic state-triggered control and cycle-level spectral design; relative to Gokul et al. [34], the increment is a topology-dependent epidemic jump–flow operator together with a network allocation law. Table 1 summarizes these distinctions without claiming that the underlying fractional or event-triggered tools are new in isolation.

Table 1. Positioning of the present framework relative to the closest fractional epidemic and event-triggered control baselines.

Study	System and Control Setting	Main Analytical/Control Object	Relation to the Present Framework
Liu et al. [33] (2022)	Fractional SIR dynamics on a two-layer weighted network; predetermined targeted immunity	Disease-free stability and structural/demographic targeting	No endogenous event trigger and no cycle-level spectral allocation rule
Liu et al. [32] (2024)	Fractional epidemic dynamics on a weighted network with time delay; infection-rate-threshold event-triggered impulses	Equilibrium stability, event-triggered impulsive control, and Zeno exclusion	Establishes fractional epidemic event triggering, but not an HIV-specific degree-correlated jump–flow operator, robust contraction family, or finite-budget Perron targeting
Gokul et al. [34] (2025)	General fractional-order switched nonlinear systems; mode-dependent event-triggered impulsive control	Finite-time/contractive stability, dwell-time conditions, and LMI design	Provides general fractional event-triggered control theory without epidemic topology or network-resource allocation
Present study	Fractional HIV dynamics on a heterogeneous degree-correlated contact network; burden-triggered screening-to-ART jumps	Matrix Mittag–Leffler jump–flow operator, robust cycle contraction, nonlinear extinction, and Perron sensitivity	Couples intervention timing, fractional memory, topology uncertainty, and finite-budget targeting within one HIV network-control framework

The remainder of the paper follows the analytical logic of the control problem. Section 2 defines the heterogeneous fractional HIV model, the campaign-renewed memory convention, and the risk-triggered jump law. Section 3 isolates the continuous fractional epidemic flow and derives the threshold and equilibrium results. Section 4 then closes the control loop by studying non-Zeno triggering, event-to-event contraction, robust stability, and Perron-based allocation. Section 5 specifies the numerical method and the theorem-to-diagnostic mapping, Section 6 reports the independently checked cycle-matrix diagnostics and illustrative control comparisons, Section 7 discusses interpretation and limitations, and Section 8 concludes the paper. Figure 1 gives a visual overview of the network, fractional flow, trigger and treatment-jump components.

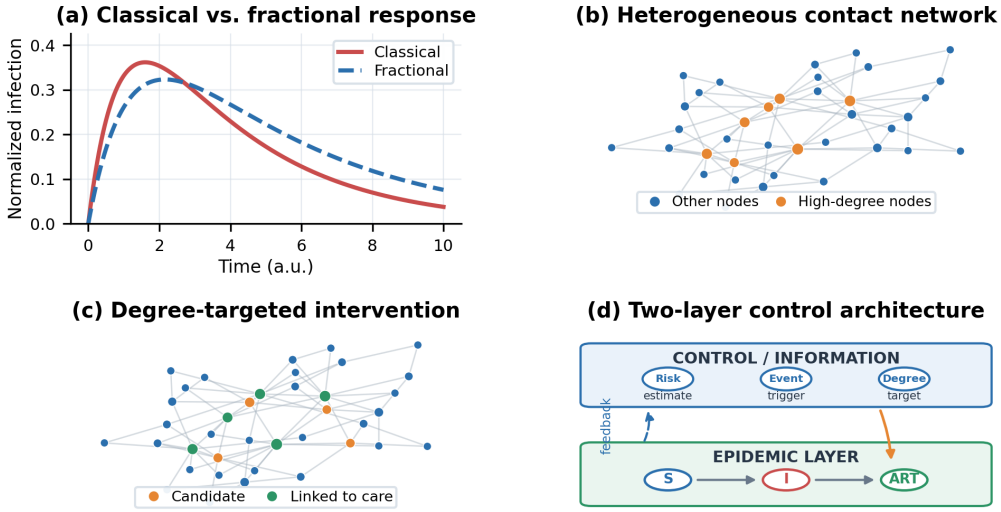


Figure 1. Stylized overview of the fractional-order HIV network-control framework, emphasizing fractional dynamics, network heterogeneity, and event-triggered targeted intervention. In panel (**d**), gray arrows denote the susceptible-to-infected-to-ART progression, the orange arrow denotes degree-targeted linkage to ART, and the blue dashed arrow denotes feedback from the epidemic layer to risk estimation and event triggering. These arrows are schematic and are not measured flows. Panel (**a**) is a qualitative illustration only, not an empirical fit or a reported simulation result.

Abbreviations and model resolution.

Antiretroviral treatment (ART) is the treated infectious class in the model; Erdős–Rényi (ER), Watts–Strogatz (WS), and Barabási–Albert (BA) denote three synthetic network generators. The state-dependent event law triggers screening and ART linkage, whereas a maximum-interval watchdog, when enabled, forces a campaign at the deadline. The living system has $3K$ class-specific variables; these are not the three undifferentiated classes of an ordinary population-wide susceptible–infected–recovered (SIR) model.

2. Fractional Heterogeneous-Network Model

2.1. Network Architecture

Let $\mathcal{K} = \{1, \dots, K\}$ denote the set of admissible degrees. The degree distribution is $P(k)$, with $\sum_k P(k) = 1$, mean degree $\langle k \rangle = \sum_k kP(k)$, and second moment $\langle k^2 \rangle = \sum_k k^2 P(k)$. Degree correlations are represented by the row-stochastic conditional mixing matrix

$$C = (C_{kk'}), \qquad C_{kk'} = P(k' \mid k), \qquad \sum_{k'} C_{kk'} = 1. \tag{1}$$

For each degree class k, $S_k(t)$, $I_k(t)$, and $T_k(t)$ denote the fractions of living individuals who are susceptible, infected and untreated, and receiving effective ART, respectively. The auxiliary variable $D_k(t)$ records cumulative HIV-related model mortality per initial degree-class population. ART reduces infectiousness by the factor $0 \le \eta < 1$. Define

$$\Theta_k(t) = \sum_{k' \in \mathcal{K}} C_{kk'}[I_{k'}(t) + \eta T_{k'}(t)]. \tag{2}$$

A susceptible individual in degree class k experiences infection pressure $\beta k \Theta_k(t)$.

2.2. Campaign-Renewed Caputo Memory

Let $0 = \tau_0 < \tau_1 < \tau_2 < \cdots$ be the intervention times. On the interval (τ_n, τ_{n+1}), the Caputo derivative is defined with lower terminal τ_n,

$$\mathcal{D}^{\alpha}_{\tau_n} x(t) = \frac{1}{\Gamma(1-\alpha)} \int_{\tau_n}^{t} (t-s)^{-\alpha} \dot{x}(s)\, ds, \qquad 0 < \alpha < 1, \tag{3}$$

We denote this operator by $\mathcal{D}^{\alpha}_{\tau_n}$ in the sequel; the usual derivative is recovered for $\alpha = 1$. This event-reset convention means that the memory kernel used by the post-campaign dynamics is referenced to the most recent intervention. It does not assert that biological history is physically erased; rather, it defines a reduced-order memory state for the intervention cycle. The full-history Caputo alternative would require a different, nonlocal jump representation and is discussed in Section 7.

Interpretation, justification, and limitation of memory renewal.

The post-campaign state is used as a new effective surveillance baseline for the subsequent screening/ART-linkage episode. This can be a useful engineering approximation when interventions substantially update the modeled cohort, follow-up information is available only from the latest campaign, and pre-campaign residual memory is negligible on the timescale of the next cycle. It does *not* mean that infection, immune, behavioral, or treatment history is biologically erased. There is presently no patient-level longitudinal evidence in the supplied data to quantify the approximation error. With a fixed initial Caputo terminal, the history prior to τ_n enters the evolution after τ_n through a nonzero memory-tail term; the post-jump point state alone is then not sufficient for the matrix factorization $JE_{\alpha}(A\Delta^{\alpha})$. Theorems 5–7 are valid only for the explicitly renewed-memory system. A finite-horizon comparison with a fixed-history impulse–Volterra convention is reported in Section 6; it is a sensitivity illustration, not a proof for full-history dynamics. A rigorous fixed-history hybrid comparison is left open.

To preserve dimensions, let τ_c be a characteristic time unit. We write the living subsystem as

$$\begin{aligned} \mathcal{D}^{\alpha}_{\tau_n} S_k &= \tau_c^{1-\alpha}[\mu(1-S_k) + \delta I_k + \delta_T T_k - \beta k S_k \Theta_k], \\ \mathcal{D}^{\alpha}_{\tau_n} I_k &= \tau_c^{1-\alpha}[\beta k S_k \Theta_k - (\mu + \delta + \gamma) I_k], \qquad t \in (\tau_n, \tau_{n+1}), \\ \mathcal{D}^{\alpha}_{\tau_n} T_k &= \tau_c^{1-\alpha}[\gamma I_k - (\mu + \delta_T) T_k], \end{aligned} \tag{4}$$

and retain cumulative mortality as the ordinary accounting equation

$$\dot{D}_k = \delta I_k + \delta_T T_k. \tag{5}$$

Here, μ is natural turnover, δ and δ_T are HIV-related mortality rates for untreated and treated infection, and γ is the background diagnosis-and-ART initiation rate. All time variables t, τ_n, h_r, $T_{\max}$ and Δ_n are measured in years, including the numerical examples. The rates β, μ, δ, δ_T, and γ have units year^{-1}, while $S_k, I_k, T_k, \Theta_k, \eta$ are dimensionless. The Caputo derivative of a dimensionless state has units year$^{-\alpha}$; hence each term $\tau_c^{1-\alpha}$ times an infection, recovery, or ART-transfer rate has the correct year$^{-\alpha}$ dimension. The ordinary death-accounting rate $\dot{D}_k$ has units year^{-1}. Throughout, $\tau_c = 1$ year. In particular, α is varied as a *sensitivity parameter*, not calibrated or inferred from the Beijing counts.

Adding the three fractional equations gives

$$\mathcal{D}^{\alpha}_{\tau_n}(S_k + I_k + T_k) = \tau_c^{1-\alpha}\mu[1 - (S_k + I_k + T_k)]. \tag{6}$$

Hence the living simplex $S_k + I_k + T_k = 1$ is invariant when it is satisfied initially.

2.3. Event-Triggered Screening and Rapid ART Linkage

Define the edge-weighted untreated burden

$$H(t) = \frac{1}{\langle k \rangle} \sum_{k \in \mathcal{K}} k P(k) I_k(t). \tag{7}$$

Let $H_{up} > 0$ be the trigger threshold and $h_r > 0$ a refractory interval. The next campaign time is

$$\tau^{\text{risk}}_{n+1} = \inf\{t \geq \tau_n + h_r : H(t) \geq H_{up}\}, \qquad \tau_{n+1} = \min\{\tau^{\text{risk}}_{n+1}, \tau_n + T_{\max}\}, \tag{8}$$

where $\inf \emptyset = +\infty$, and the watchdog branch is enabled only in scenarios that explicitly enforce Assumption 5, with $T_{\max} \geq h_r$. If the threshold is not reached by the deadline, the watchdog *must* initiate a campaign using the same specified jump U_{n+1}; it does not merely end a theoretical observation interval. In the limit where the watchdog is disabled, the second term in the minimum is omitted and a finite upper inter-event interval is no longer guaranteed. All campaign counts and treatment-transfer effort must then include watchdog-forced campaigns. The regenerated nonlinear experiment in Section 6 logs both risk-triggered and watchdog-forced events, and it separately reports campaign count, nominal pulse effort and actual ART transfers. At $t = \tau_n$, a fraction $u_{k,n}$ of untreated infection in degree class k is linked immediately to ART:

$$\begin{aligned} S_k(\tau_n^+) &= S_k(\tau_n^-), \\ I_k(\tau_n^+) &= (1 - u_{k,n}) I_k(\tau_n^-), \\ T_k(\tau_n^+) &= T_k(\tau_n^-) + u_{k,n} I_k(\tau_n^-), \\ D_k(\tau_n^+) &= D_k(\tau_n^-). \end{aligned} \tag{9}$$

The jump conserves the living population and does not directly alter cumulative mortality.

2.4. Basic Assumptions and Well-Posedness

We use the following assumptions.

Assumption 1. *$P(k) > 0$ on the finite degree support and $C = [C_{kk'}]$ is irreducible and row-stochastic.*

Assumption 2. *All epidemiological parameters are non-negative, with the removal and treatment rates required in the denominators strictly positive.*

Assumption 3. *Campaign intensities are measurable and satisfy $0 \leq u_k \leq 1$.*

Assumption 4. *The refractory interval satisfies $h_r > 0$.*

Assumption 5. *For the continuous-time stability results of Theorems 5–7, a watchdog rule enforces a uniform dwell-time window $h_r \leq \Delta_n = \tau_{n+1} - \tau_n \leq T_{\max} < \infty$.*

The upper bound in Assumption 5 is not needed for positivity or Zeno exclusion; it is required only to convert geometric contraction in the event index into a uniform decay estimate in physical time.

Proposition 1 (positivity and invariance)**.** *For every admissible initial state, system (4)–(9) admits a unique piecewise-continuous solution on every finite time interval. Uniqueness is first established for each renewed-memory Volterra interval and then extended to the hybrid path by uniquely concatenating the specified jumps. The living variables remain non-negative, the simplex $S_k + I_k + T_k = 1$ is invariant, and each $D_k(t)$ is nondecreasing.*

Proof. Fix an inter-event interval $[\tau_n, \tau_{n+1})$. With the campaign-renewed lower terminal τ_n, system (4)–(9) is equivalent to the Volterra equation

$$x(t) = x(\tau_n) + \frac{1}{\Gamma(\alpha)} \int_{\tau_n}^{t} (t - s)^{\alpha - 1} f(x(s))\, ds.$$

Local Lipschitz continuity of f gives a unique local solution. On each boundary face of the positive cone, every loss term containing the vanishing component disappears while the

remaining inflow terms are non-negative; the fractional comparison principle therefore preserves non-negativity. Summing S_k, I_k, and T_k cancels all internal infection and treatment-transfer terms and preserves the living simplex. At an intervention time, $I_k^+ = (1-u_k)I_k^-$ and $T_k^+ = T_k^- + u_k I_k^-$ are positive and mass preserving. Finally, the refractory interval $h_r > 0$ yields $\tau_{n+1} - \tau_n \geq h_r$, so event times cannot accumulate on a finite interval. Hence the inter-event solutions and jumps can be concatenated uniquely on every finite time horizon, proving positivity, invariance, and hybrid well-posedness. □

3. Fractional Threshold Dynamics and Mittag–Leffler Stability

3.1. Disease-Free State and Reproduction Number

The disease-free living equilibrium is

$$S_k^* = 1, \qquad I_k^* = T_k^* = 0. \tag{10}$$

Let $M = diag(k)C$, and define the positive transition rates $a := \mu + \delta + \gamma$ and $b := \mu + \delta_T$. Linearization of the infected–treated subsystem at (10) yields

$$\mathcal{D}^{\alpha}_{\tau_n} x = \tau_c^{1-\alpha} A x, \qquad x = (I_1, \dots, I_K, T_1, \dots, T_K)^{\top}, \tag{11}$$

where

$$A = \begin{pmatrix} \beta M - aI_K & \beta\eta M \\ \gamma I_K & -bI_K \end{pmatrix}. \tag{12}$$

The next-generation operator is unchanged by the commensurate memory order because the equilibrium infection-production and transition operators retain the same algebraic decomposition used in heterogeneous epidemic threshold theory [35,36]. Therefore

$$\mathcal{R}_0 = \frac{\beta(b+\eta\gamma)}{ab}\rho(M). \tag{13}$$

For uncorrelated mixing, $C_{kk'} = k'P(k')/\langle k\rangle$ and

$$\rho(M) = \frac{\langle k^2\rangle}{\langle k\rangle}, \qquad \mathcal{R}_0 = \frac{\beta(b+\eta\gamma)}{ab}\frac{\langle k^2\rangle}{\langle k\rangle}. \tag{14}$$

Thus α changes the transient memory law but not the algebraic invasion threshold.

3.2. Local Mittag–Leffler Stability

Theorem 1 (fractional threshold stability)**.** *The disease-free living equilibrium is locally Mittag–Leffler stable if* $\mathcal{R}_0 < 1$ *and unstable if* $\mathcal{R}_0 > 1$*, for every* $0 < \alpha \leq 1$.

Proof. The infected–treated linearization is Metzler. Its spectral bound is negative if and only if $\mathcal{R}_0 < 1$, by the next-generation characterization in Section 3.1 and standard non-negative-matrix theory [37]. In that case every eigenvalue λ of A satisfies $|\arg(\lambda)| > \alpha\pi/2$ for $0 < \alpha \leq 1$, so the Matignon sector criterion and Mittag–Leffler stability theory imply local asymptotic Mittag–Leffler stability [15,16]. If $\mathcal{R}_0 > 1$, the Metzler matrix has a positive real spectral value; the sector condition fails and the disease-free equilibrium is unstable for every admissible α. □

This result separates two roles: the network and epidemiological parameters decide whether invasion is possible, while the fractional order controls how the transient approaches or departs from the equilibrium.

3.3. Global Fractional Extinction

Because $0 \le S_k \le 1$, the nonlinear infected–treated subsystem is componentwise dominated by (11). For a Hurwitz Metzler matrix A, there exists $w \gg 0$ and $c > 0$ such that $Aw \le -cw$.

Theorem 2 (extinction for an uninterrupted Caputo episode). *If $\mathcal{R}_0 < 1$, the disease-free state is globally attractive for the* uninterrupted *fractional living flow with fixed lower terminal t_0. There exist $w \gg 0$ and $c > 0$, depending on the fixed parameters, such that for $t \ge t_0$,*

$$\|x(t)\|_{w,\infty} \le E_\alpha\big(-\tau_c^{1-\alpha} c (t-t_0)^\alpha\big)\|x(t_0)\|_{w,\infty}, \qquad \|x\|_{w,\infty} := \max_i |x_i|/w_i. \tag{15}$$

Repeated memory resets and treatment jumps require a separate cycle estimate and are covered by Theorem 6 when its hypotheses hold.

Proof. Write the infected–treated system as $\mathcal{D}^\alpha_{t_0} x = \tau_c^{1-\alpha}(Ax - h(t))$, where the first K components of $h(t)$ equal $\beta k[1 - S_k(t)]\Theta_k(t) \ge 0$ and the remaining components vanish. The positive Metzler matrix resolvent gives the variation-of-constants identity

$$x(t) = E_\alpha(\tau_c^{1-\alpha} A (t-t_0)^\alpha) x(t_0) - \tau_c^{1-\alpha} \int_{t_0}^{t} (t-s)^{\alpha-1} E_{\alpha,\alpha}(\tau_c^{1-\alpha} A (t-s)^\alpha) h(s)\, ds.$$

For a Metzler generator, both the free-flow and forcing resolvent kernels are componentwise non-negative. Thus, without assuming that the nonlinear infected–treated subsystem itself is cooperative, $0 \le x(t) \le E_\alpha(\tau_c^{1-\alpha} A (t-t_0)^\alpha) x(t_0)$. If $\mathcal{R}_0 < 1$, A is Hurwitz and Metzler, so there exist $w \gg 0$ and $c > 0$ satisfying $Aw \le -cw$; positivity of the fractional resolvent then implies $E_\alpha(\tau_c^{1-\alpha} A t^\alpha) w \le E_\alpha(-\tau_c^{1-\alpha} c t^\alpha) w$. Taking the monotone weighted infinity norm proves the bound. For $0 < \alpha < 1$ its tail is generally algebraic, not exponential. □

3.4. Endemic Living State

The equilibrium equations of the living subsystem do not contain α. Hence the existence and uniqueness problem reduces to the same algebraic fixed-point equation as in the classical model.

Theorem 3 (unique endemic state under uncorrelated mixing). *For an uncorrelated degree network with $P(k) > 0$, the reduced living subsystem has no positive endemic equilibrium if $\mathcal{R}_0 \le 1$ and has exactly one positive endemic equilibrium if $\mathcal{R}_0 > 1$.*

Proof. Under uncorrelated mixing, let Θ^* denote the equilibrium probability that a contacted neighbor is untreated or effectively infectious. Put $q = 1 + \eta\gamma/b$, $r = 1 + \gamma/b$, and $c_k(\Theta) = \beta k \Theta / a$. Solving the stationary class equations together with $S_k + I_k + T_k = 1$ gives

$$S_k^* = \frac{1}{1 + r c_k(\Theta^*)}, \qquad I_k^* = \frac{c_k(\Theta^*)}{1 + r c_k(\Theta^*)}, \qquad T_k^* = \frac{(\gamma/b) c_k(\Theta^*)}{1 + r c_k(\Theta^*)}.$$

Hence $I_k^* + \eta T_k^* = q c_k(\Theta^*)/[1 + r c_k(\Theta^*)]$. The consistency condition is $\Theta^* = F(\Theta^*)$, where

$$F(\Theta) = \sum_k \frac{k P(k)}{\langle k \rangle} \frac{q c_k(\Theta)}{1 + r c_k(\Theta)}.$$

Direct differentiation yields $F(0) = 0$, $F'(0) = \mathcal{R}_0$, $F'(\Theta) > 0$, and $F''(\Theta) < 0$ for $\Theta > 0$. Because each term in F is bounded by its contact weight and $\eta \le 1$, F maps the admissible interval into itself. If $\mathcal{R}_0 \le 1$, strict concavity gives $F(\Theta) < \Theta$ for every $\Theta > 0$, so no positive equilibrium exists. If $\mathcal{R}_0 > 1$, $F(\Theta) - \Theta$ is positive for sufficiently small $\Theta > 0$ and nonpositive at the upper endpoint of the admissible interval; continuity gives a positive fixed point and strict concavity makes it unique. Substitution into the formulas above yields the unique endemic living state. □

Section 3 has therefore separated the uncontrolled fractional-flow problem into three pieces: an invasion threshold, a global disease-free extinction condition, and an endemic fixed-point alternative. The next step is different in kind. Section 4 asks whether a state-triggered intervention can stabilize the system even when the uncontrolled flow is super-critical, and it does so at the level of the complete fractional flow–jump cycle.

4. Fractional Event-Triggered Hybrid Control: Jump–Flow Contraction, Robustness, and Targeting

4.1. Matrix Mittag–Leffler Flow

For a fixed inter-event interval $\Delta_n = \tau_{n+1} - \tau_n$, the linearized post-campaign flow is

$$x(\tau_{n+1}^-) = F_\alpha(\Delta_n)x(\tau_n^+). \tag{16}$$

$$F_\alpha(\Delta) = E_\alpha(\tau_c^{1-\alpha} A\Delta^\alpha). \tag{17}$$

Lemma 1 (positivity and compact boundedness of the fractional flow)**.** *If A is Metzler, then $F_\alpha(\Delta)$ is entrywise non-negative for every $\alpha \in [\alpha_-, 1]$ and $\Delta \in [0, T_{\max}]$. Moreover, the map $(\alpha, \Delta) \mapsto F_\alpha(\Delta)$ is continuous on the compact set $[\alpha_-, 1] \times [0, T_{\max}]$, and therefore*

$$M_F := \sup_{\alpha\in[\alpha_-,1], 0\le\Delta\le T_{\max}} \| F_\alpha(\Delta) \|_* < \infty. \tag{18}$$

Proof. The matrix Mittag–Leffler function is defined by a power series that converges uniformly on compact subsets of its matrix argument and, for α bounded away from zero, uniformly over compact α-intervals; this gives continuity in (α, Δ, A) [12–14]. For a Metzler matrix A, positivity of the Caputo comparison system implies $E_\alpha(A\Delta^\alpha) \ge 0$ entrywise for $\Delta \ge 0$. Continuity on the compact admissible parameter set then gives a finite uniform induced-norm bound. This positivity-and-boundedness pair is the fractional substitute for the positive-semigroup estimate used in ordinary hybrid systems. □

Let

$$J(U_n) = \begin{pmatrix} I_K - U_n & 0 \\ U_n & I_K \end{pmatrix}, \qquad U_n = diag(u_{1,n}, \dots, u_{K,n}). \tag{19}$$

The event-to-event map becomes

$$x(\tau_{n+1}^+) = \mathcal{G}_\alpha(U_{n+1}, \Delta_n)x(\tau_n^+). \tag{20}$$

$$\mathcal{G}_\alpha(U, \Delta) = J(U)F_\alpha(\Delta). \tag{21}$$

At $\alpha = 1$, $E_1(A\Delta) = e^{A\Delta}$ and (21) reduces exactly to the classical jump–flow operator.

Corollary 1 (integer-order consistency)**.** *For every fixed admissible A, J, and Δ,*

$$\lim_{\alpha\to 1^-} JE_\alpha(A\Delta^\alpha) = J\exp(A\Delta).$$

Hence the proposed fractional hybrid-control criterion continuously recovers the standard integer-order jump–flow stability condition. This limiting property shows that the new theory extends, rather than replaces, classical event-triggered impulsive control.

4.2. Exclusion of Zeno Behavior

Theorem 4 (non-Zeno triggering)**.** *Under (8), $\tau_{n+1} - \tau_n \ge h_r > 0$. Hence the event sequence has no finite accumulation point and the number of campaigns over a finite horizon T satisfies $N(T) \le 1 + T/h_r$.*

Proof. By construction, after an event at τ_n the trigger is disabled on $[\tau_n, \tau_n + h_r)$. Therefore $\tau_{n+1} - \tau_n \geq h_r$ for every n, independently of the memory order, and finite event accumulation is impossible. If $N(T)$ denotes the number of campaigns on $[0, T]$, then $N(T) \leq 1 + T/h_r$. Thus the refractory window supplies an explicit Zeno-exclusion certificate, paralleling the role of lower inter-event bounds in event-triggered and impulsive-control theory [20–27]. Assumption 5 adds only an upper watchdog interval for Theorems 5–7 and does not alter this lower-bound argument. □

4.3. Uniform Fractional Jump–Flow Contraction

Let $\mathcal{U}$ be a compact set of admissible campaign matrices, $\alpha \in [\alpha_-, 1]$, and $\Delta \in [T_{\min}, T_{\max}]$.

Theorem 5 (uniform fractional cycle contraction)**.** *Suppose there exists one monotone vector norm $\|\cdot\|_*$, fixed independently of α, U, and Δ, and a constant $q \in (0,1)$ such that*

$$\sup_{\alpha \in [\alpha_-, 1],\, U \in \mathcal{U},\, \Delta \in [T_{\min}, T_{\max}]} \| J(U) E_\alpha\left(\tau_c^{1-\alpha} A \Delta^\alpha\right) \|_* \leq q < 1. \tag{22}$$

Then the repeatedly renewed hybrid *system admits an exponential* envelope in physical time *measured from the first post-campaign state $x(\tau_0^+)$. More precisely, there exist $C \geq 1$ and $\xi > 0$ independent of the admissible campaign sequence such that*

$$\| x(t) \|_* \leq C e^{-\xi (t - \tau_0)} \| x\left(\tau_0^+\right) \|_*, \quad t \geq \tau_0. \tag{23}$$

Proof. For the nth admissible cycle define

$$\Psi_n = J(U_n) E_{\alpha_n}\left(\tau_c^{1-\alpha_n} A \Delta_n^{\alpha_n}\right),$$

where A is the fixed disease-free comparison matrix. The hypothesis supplies the same monotone norm for every admissible cycle, with $\|\Psi_n\|_* \leq q < 1$, hence $\|x(\tau_n^+)\|_* \leq q^n \|x(\tau_0^+)\|_*$. Let

$$M_F = \sup_{\alpha \in [\alpha_-, 1],\, 0 \leq s \leq T_{\max}} \left\| E_\alpha\left(\tau_c^{1-\alpha} A s^\alpha\right) \right\|_* < \infty,$$

which follows from compact-set continuity of the Mittag–Leffler flow. For $t \in [\tau_n, \tau_{n+1})$, $\|x(t)\|_* \leq M_F q^n \|x(\tau_0^+)\|_*$. Assumption 5 gives $\Delta_j \leq T_{\max}$, so

$$t < \tau_{n+1} = \tau_0 + \sum_{j=0}^{n} \Delta_j \leq \tau_0 + (n+1) T_{\max}.$$

Therefore $n > (t - \tau_0)/T_{\max} - 1$ and $q^n \leq q^{-1} \exp[-|\log q|(t - \tau_0)/T_{\max}]$. Consequently,

$$\|x(t)\|_* \leq \frac{M_F}{q} \exp\left[-\frac{|\log q|}{T_{\max}} (t - \tau_0)\right] \|x(\tau_0^+)\|_*.$$

The conversion from event-index contraction to physical-time decay is thus explicit and uses the watchdog upper interval essentially; no exponential-semigroup approximation of the fractional flow is made. □

Theorem 5 is stronger than disease-free stability of the uncontrolled fractional system. It permits the uncontrolled flow to be supercritical, provided repeated interventions make the complete cycle contractive. The exponential estimate in (23) is a property of the repeated campaign-renewed hybrid trajectory; it is not a claim of exponential decay for one uninterrupted Caputo flow, whose natural decay law is Mittag–Leffler.

Remark 1 (design interpretation of the contraction test)**.** *Condition* (22) *is directly actionable for intervention design. Given a family of feasible trigger thresholds and class-dependent campaign intensities, one can evaluate the largest admissible norm of the jump–flow operator on the uncertainty box* $[\alpha_-, 1] \times \mathcal{U} \times [T_{\min}, T_{\max}]$*. A verified margin* $q < 1$ *is then a certificate that every admissible campaign sequence is stabilizing, whereas* $q > 1$ *indicates that either the intervention intensity must be increased or the maximal inter-event interval must be reduced.*

Remark 2 (computable common-norm criterion)**.** *For non-negative cycle matrices* $G(\omega)$ *and a positive vector* w*,*

$$\|G(\omega)\|_{w,\infty} = \max_i \frac{[G(\omega)w]_i}{w_i}, \qquad G(\omega)w \le qw \text{ componentwise.} \tag{24}$$

Thus a common *certificate can be searched for by fixing* $q < 1$ *and solving linear feasibility inequalities in* w *over a prescribed finite family. For a compact continuum, checking only finitely many mesh points is insufficient: a validated interval enclosure or another uniform analytic bound on the unexamined region is needed. In particular,* $\rho(G(\omega)) < 1$ *for every individual matrix does* not *imply arbitrary-switching stability. An explicit six-mode finite-family certificate with its common* w*, full parameter set, and executable matrix code is reported in Section 5.5.*

4.4. Nonlinear Global Extinction Under Cycle Contraction

Theorem 6 (nonlinear hybrid extinction without nonlinear cooperativity)**.** *Assume the hypotheses of Theorem 5, including a fixed common monotone norm, the renewed-memory dynamics, and watchdog-enforced bounded cycles. For the model in* (4)*, every admissible nonlinear solution converges to the disease-free manifold, and the aggregate cumulative mortality has a finite limit. No cooperativity assumption on the* nonlinear *infected–treated vector field is required.*

Proof. On every interval $[\tau_n, \tau_{n+1})$, set $x = (I_1, \dots, I_K, T_1, \dots, T_K)^\top \ge 0$ and $h_k(t) = \beta k(1 - S_k(t))\Theta_k(t)$ for $1 \le k \le K$, with $h_{K+k}(t) = 0$. Since $0 \le S_k \le 1$ and $\Theta_k \ge 0$, $h(t) \ge 0$, and the true subsystem equals $\mathcal{D}^\alpha_{\tau_n} x = \tau_c^{1-\alpha}(Ax - h(t))$. The variation-of-constants formula used in Theorem 2 and positivity of the Mittag–Leffler resolvent imply

$$0 \le x(\tau_{n+1}^-) \le E_\alpha(\tau_c^{1-\alpha} A \Delta_n^\alpha) x(\tau_n^+).$$

The treatment jump $J(U) \ge 0$ preserves the componentwise order. Induction bounds each nonlinear post-jump state by the product of the corresponding positive *linear* jump–flow matrices, for which the common norm bound $q < 1$ holds. Combining this with the uniform inter-event flow bound M_F and the watchdog estimate of Theorem 5 gives the same physical-time hybrid envelope. This establishes $I_k(t), T_k(t) \to 0$ and, since $S_k + I_k + T_k = 1$, $S_k(t) \to 1$. The ordinary accounting equation $\dot{D}_k = \delta I_k + \delta_T T_k$ has a non-negative integrable right-hand side under the hybrid envelope, so every D_k has a finite limit. Crucially, the nonlinear Jacobian is *not* asserted to be Metzler; all comparisons are made against the positive linear operator A through a non-negative forcing kernel. □

4.5. Robust Fractional Control Under Memory, Topology, and Timing Uncertainty

Let $\mathcal{C}$ be a compact set of irreducible row-stochastic mixing matrices, Θ a compact epidemiological parameter set, and $\mathcal{J}$ the associated compact set of admissible jump matrices. Assume that $(\theta, C) \mapsto A_{\theta,C}$ is continuous and that a single positive weight vector w defines the same weighted infinity norm throughout the uncertainty set. Define

$$\Omega = [\alpha_-, 1] \times \mathcal{C} \times \Theta \times \mathcal{J} \times [T_{\min}, T_{\max}].$$
$$\Gamma_F = \sup_{(\alpha, C, \theta, J, \Delta) \in \Omega} \| J E_\alpha\left(\tau_c^{1-\alpha} A_{\theta,C} \Delta^\alpha\right) \|_{w,\infty}. \tag{25}$$

Theorem 7 (uniform robust fractional contraction)**.** *Assume that every $A_{\theta,C}$ is Metzler, the infected–treated nonlinear system can be written interval-wise as $\mathcal{D}^{\alpha}x = \tau_c^{1-\alpha}(A_{\theta,C}x - h_{\theta,C}(t))$ with $h_{\theta,C}(t) \geq 0$, and every jump matrix is non-negative. If $\Gamma_F < 1$, then the disease-free manifold is uniformly globally attractive in the living variables for every admissible fractional order, topology, parameter realization, and flow–jump sequence. The decay constants can be chosen independently of the uncertainty realization. For the present HIV model, the domination hypothesis is satisfied uniformly whenever the uncertainty set preserves non-negative parameters and $0 \leq S_k \leq 1$, because $\beta k S_k \Theta_k \leq \beta k \Theta_k$.*

Proof. Let $\Omega = [\alpha_-, 1] \times \mathcal{C} \times \Theta \times \mathcal{J} \times [T_{\min}, T_{\max}]$ and define

$$\Psi(\omega) = JE_{\alpha}\big(\tau_c^{1-\alpha} A_{\theta,C} \Delta^{\alpha}\big).$$

Because $\alpha_- > 0$ and $A_{\theta,C}$ ranges over a compact matrix family, the defining Mittag–Leffler series converges uniformly on Ω; standard compact-set properties of Mittag–Leffler functions therefore make $\omega \mapsto \Psi(\omega)$ continuous [13,14]. The common weight vector w makes $\omega \mapsto \|\Psi(\omega)\|_{w,\infty}$ continuous as well. Since Ω is compact, the worst-case gain Γ_F is attained. If $\Gamma_F < 1$, choose q with $\Gamma_F < q < 1$. Every admissible cycle then satisfies the same contraction inequality, and compactness also provides a common bound M_F for the inter-event flow. The argument of Theorem 5 therefore yields decay constants independent of the realized α, topology, epidemiological parameters, jump matrix, and trigger interval. Under the uniform non-negative forcing condition, the positive Mittag–Leffler resolvent comparison in Theorem 6 transfers the same envelope to the nonlinear infected–treated subsystem, which proves uniform global attraction of the disease-free manifold. The robustness statement is intentionally limited to compact uncertainty sets admitting a common weighted norm, a uniform comparison relation, and a strict margin $\Gamma_F < 1$; outside these conditions the theorem makes no uniform claim. □

State-space scalability and clinical-compartment extension.

For the present K-class construction, the living system already has $3K$ states and the infected–treated comparison operator is $2K \times 2K$; thus, at $K = 40$, the analysis is carried out in 120 living dimensions, not a three-scalar susceptible–infected–recovered (SIR) model. This high-dimensional *degree stratification* should not be confused with having more than five distinct HIV clinical compartments. For a future m-dimensional infected clinical-state extension, a sufficient abstract structure is

$$\mathcal{D}^{\alpha}_{\tau_n} z = \tau_c^{1-\alpha}\big(B_{\vartheta} z - h_{\vartheta}(t)\big), \quad z \geq 0,\ h_{\vartheta}(t) \geq 0, \quad B_{\vartheta} \text{ Metzler}, \qquad z(\tau_n^{+}) = J_n z(\tau_n^{-}), \quad J_n \geq 0. \tag{26}$$

If the state remains non-negative, the fractional resolvent kernels for B_{ϑ} are positive, and a *single* vector $w \gg 0$ verifies $J_n E_{\alpha}(\tau_c^{1-\alpha} B_{\vartheta} \Delta_n^{\alpha}) w \leq qw$ with $q < 1$ throughout a declared admissible family, then the same variation-of-constants comparison and bounded-cycle argument as in Theorems 5–7 applies in dimension m. This is a conditional structural extension, not a claim that positivity, a suitable comparison residual, common weights, or credible rates have been verified for any specific six-clinical-compartment HIV model. More compartments require a newly specified biology and a fresh check of each condition.

4.6. Perron Spectral-Sensitivity Targeting Under Budget Constraints

Degree-only targeting is intuitive on an uncorrelated network, but it can be suboptimal when degree correlations redistribute the dominant transmission mode. Consider a fixed α and Δ and let

$$G_{\alpha}(U) = J(U) F_{\alpha}(\Delta). \tag{27}$$

Assume its Perron root $\rho(G_{\alpha})$ is simple, with positive right and left eigenvectors r and ℓ normalized so that $\ell^{\top} r = 1$.

Proposition 2 (first-order spectral targeting score)**.** *For a small change in class-k campaign intensity,*

$$\frac{\partial \rho(G_\alpha)}{\partial u_k} = \ell^\top \frac{\partial J}{\partial u_k} F_\alpha(\Delta) r. \tag{28}$$

Define the raw marginal reduction in the dominant fractional cycle gain by

$$s_k^{(\alpha)} = -\frac{\partial \rho(G_\alpha)}{\partial u_k}. \tag{29}$$

Proof. Because the Perron root is simple and $\ell^\top r = 1$, standard simple-eigenvalue perturbation gives $\partial\rho/\partial u_k = \ell^\top(\partial G_\alpha/\partial u_k)r$. Since $F_\alpha(\Delta)$ is independent of u_k for the fixed-flow sensitivity calculation, $\partial G_\alpha/\partial u_k = (\partial J/\partial u_k)F_\alpha(\Delta)$, which yields (28). Definition (29) changes the sign so that positive $s_k^{(\alpha)}$ denotes a first-order reduction in the dominant cycle gain. □

The corresponding benefit per unit cost is $s_k^{(\alpha)}/c_k$. The distinction is important: $s_k^{(\alpha)}$ is the raw first-order decrease in the dominant cycle gain, whereas division by c_k is used only when allocating a finite intervention budget. On an uncorrelated network the two rankings can be strongly degree aligned under homogeneous costs, while assortative or disassortative mixing changes the left–right Perron geometry and can reorder the preferred targets.

Remark 3 (degree-aligned limiting case)**.** *Under uncorrelated mixing, homogeneous intervention costs, and a weak-perturbation/leading-mode approximation, the Perron sensitivity is degree aligned because the dominant transmission mode is generated by the size-biased degree distribution. This observation explains why high-degree targeting is a useful proxy in the uncorrelated benchmark. It is not asserted as a universal monotonicity theorem: correlated mixing, heterogeneous costs, or finite interventions can change the ranking.*

Proposition 3 (budget-constrained greedy allocation)**.** *Assume that the nominal cycle matrix $G_\alpha(U^0)$ has a simple Perron root. Consider an incremental budget $B > 0$ applied around the nominal pulse U^0, with admissible changes $0 \le \Delta u_k \le \bar{u}_k - u_k^0$ and weighted cost $\sum_k c_k \Delta u_k \le B$. Maximizing the first-order decrease in the dominant cycle gain,*

$$\max \sum_k s_k^{(\alpha)} \Delta u_k, \qquad \text{subject to } \sum_k c_k \Delta u_k \le B,$$

is solved at first order by allocating admissible increments in decreasing order of the benefit–cost ratio $s_k^{(\alpha)}/c_k$ until the budget is exhausted or a class-specific upper bound becomes active.

Proof. Let $M(U) = J(U)E_\alpha(\tau_c^{1-\alpha} A \Delta^\alpha)$ have a simple Perron root ρ with normalized positive left and right eigenvectors w and v, $w^\top v = 1$. Standard simple-eigenvalue perturbation gives

$$\frac{d\rho}{du_k} = w^\top \frac{\partial M}{\partial u_k} v,$$

so Proposition 2 defines the raw benefit $s_k^{(\alpha)} = -d\rho/du_k$. For the linearized incremental problem, the first-order decrease in ρ is $\sum_k s_k^{(\alpha)} \Delta u_k$, subject to $\sum_k c_k \Delta u_k \le B$ and the box constraints. This is the continuous fractional-knapsack problem: an optimum is obtained by filling admissible increments in descending order of $s_k^{(\alpha)}/c_k$ until the budget is exhausted or an upper bound becomes active. The result is explicitly first-order; it does not claim global optimality for the original nonlinear hybrid-control problem. It is valid while the nominal Perron root remains simple. At an eigenvalue crossing or at a reducible boundary configuration, the derivative formula must be replaced by a one-sided/subgradient or finite-difference sensitivity analysis. □

Remark 4 (relation to static targeted-immunity policies)**.** *The intervention layer is not algebraically identical to the weighted-network SIR controller of Liu et al. [33], because the disease states, jump mechanism, and control objective differ. If, however, the risk trigger is replaced by a permanently active structural selector and U is fixed from a network threshold, the timing layer collapses to a static topology-based policy in the same design spirit. The present framework extends that regime by making intervention timing endogenous and by optimizing the spectral radius of the complete fractional jump–flow operator rather than a static transition rate alone.*

Assumption audit for the hybrid-control results.

The logical dependence of the control results is explicit. Theorem 4 requires only the positive refractory window in Assumption 4. Theorem 5 additionally requires the upper watchdog interval in Assumption 5 and one common monotone norm, independent of memory order, pulse, and inter-event time, in which every admissible cycle satisfies (22). Theorem 6 uses the componentwise inequality $h(t) \geq 0$, the non-negative fractional resolvent kernel, and a positive jump map; nonlinear cooperativity is neither assumed nor generally true. Theorem 7 requires those comparison properties uniformly over compact uncertainty sets, continuity of $(\theta, C) \mapsto A_{\theta,C}$, one common weighted norm over the entire family, a non-negative forcing residual, and the strict margin $\Gamma_F < 1$. Propositions 2 and 3 are local first-order results and require a simple Perron root at the nominal design point; they are not asserted across eigenvalue crossings or reducible boundary cases. Finally, the event-to-event factorization behind Theorems 5–7 depends on the campaign-renewed Caputo convention and is not transferred without modification to the fixed-history formulation examined only as a sensitivity benchmark in Section 6.

The analysis in Section 4 yields three quantities that can be checked numerically without changing the model: the spacing of trigger events, the gain of the fractional cycle operator, and the Perron sensitivity of that gain to class-specific intervention. Section 5 therefore defines the numerical method and parameters around these quantities, and Section 6 uses them as the organizing diagnostics for the simulations.

5. Numerical Methods, Parameterization, and Diagnostic Structure

5.1. Fractional Predictor–Corrector Integration with Event Restart

On each inter-event interval, the Caputo subsystem is integrated with the predictor–corrector Adams–Bashforth–Moulton product-integration method of Diethelm, Ford, and Freed [38], a standard approach for fractional differential equations whose numerical properties and implementations are reviewed by Garrappa [39]. For a scalar representation with step h, the predictor is

$$y_{n+1}^{P} = y_0 + \frac{h^{\alpha}}{\Gamma(\alpha+1)} \sum_{j=0}^{n} [(n+1-j)^{\alpha} - (n-j)^{\alpha}] f_j, \tag{30}$$

and the corrector is

$$y_{n+1} = y_0 + \frac{h^{\alpha}}{\Gamma(\alpha+2)} \left[f\left(t_{n+1}, y_{n+1}^{P}\right) + \sum_{j=0}^{n} a_{j,n+1} f_j \right], \tag{31}$$

with the standard Diethelm weights [38,39]. When the trigger condition is met, the jump (9) is applied and a new Caputo segment is initialized from the post-jump state. This implements the campaign-renewed memory convention directly rather than approximating a full-history impulsive model.

5.2. Baseline Network and Parameters

The baseline degree law is a truncated power law $P(k) \propto k^{-2.7}$ for $k = 1, \ldots, 40$. Unless otherwise stated, uncorrelated mixing is used. Annual parameters are

$$\mu = 0.012, \quad \delta = 0.035, \quad \delta_T = 0.008, \quad \gamma = 0.18, \quad \eta = 0.12, \quad \beta = 0.09. \tag{32}$$

The initial untreated state is degree dependent,

$$I_k(0) = 0.004\left(\frac{k}{K}\right)^{1/2}, \qquad T_k(0) = 0, \qquad S_k(0) = 1 - I_k(0). \tag{33}$$

The baseline trigger uses $H_{up} = 0.003$ and $h_r = 1$ year. For the separately declared active-trigger nonlinear validation in Section 6 we vary only the control timing to $H_{up} = 0.0018$, $h_r = 0.25$ years, $T_{\max} = 2$ years and use a 20-year horizon and $h = 0.05$-year grid (with smaller steps for convergence checks). The degree-targeted pulse is

$$u_k = \min\left\{u_{\max},\ 0.15 + (u_{\max} - 0.15)\left(\frac{k}{K}\right)^{1.25}\right\}, \qquad u_{\max} = 0.65. \tag{34}$$

The baseline $\beta = 0.09$ is deliberately supercritical: for the stated degree distribution and rates, $\rho(M) = 3.76955452$ and $\mathcal{R}_0 = 3.10863703$. The one-cycle spectrum of the baseline degree-pulse policy is $\rho(G_{0.85}(U, 1\text{ year})) = 1.06881753 > 1$; this policy therefore has *no* certified contraction margin. We use a *separate*, clearly labeled certificate example with $\beta = 0.036$ and $u_k = 1$ to demonstrate a possible contractive flow–jump family. This theoretical example is not a calibration or recommended intervention intensity in practice.

5.3. Numerical Diagnostics

The revised numerical diagnostics distinguish finite-horizon trajectory reductions from a genuine uniform-contraction certificate. The reproducibility materials document the numerical algorithms, numerical inputs, and seeded synthetic-network draws. The simulation evidence is finite-horizon and does not replace the common-norm hypotheses of Theorems 5–7.

The following table maps the principal mathematical statements to their numerical diagnostics and states the limits of the evidence. Table 2 provides the summary.

Table 2. What is, and is not, demonstrated by the evidence.

Mathematical or Modeling Statement	Testable Quantity	Evidence and Scope
$\mathcal{R}_0$ threshold and Theorem 2	Positive infection operator and uncompelled Mittag–Leffler flow	Exact disease-free linearization; theorem applies to uninterrupted episodes
Theorems 5 and 6	One *common* induced norm of all admissible cycle matrices	Explicit six-mode certificate in Section 5.5; not validated for the baseline pulse
Theorem 7	One weight valid throughout a declared compact uncertainty family	Conditional theorem; 100 synthetic networks alone do not certify the continuum
Spectral sensitivity	Dimensionless local sensitivity of the one-cycle gain	Independently computed by central ±1% perturbations of the exact cycle-gain operator

Table 2. *Cont*.

Mathematical or Modeling Statement	Testable Quantity	Evidence and Scope
Memory convention	Renewal versus fixed-history fractional response	Qualitative sensitivity illustration, not an equivalence theorem
Surveillance data	Aggregate Beijing monthly trends	Descriptive temporal context only; no identification of α, topology or intervention effect

5.4. Reproducibility, Numerical Limitations, and Controlled Comparisons

The accompanying Supplementary Materials (Supplementary Code S1 and Supplementary Data S1) provide the executable scripts and machine-readable inputs and outputs. The script `reproducible_cycle_audit.py` independently reconstructs the 80-dimensional linear flow–jump spectral operator and records the baseline audit and six-mode common-weight certificate. The script `reproduce_nonlinear_and_networks.py` implements the fractional predictor–corrector integrator with a compulsory watchdog and records event times, event reasons, cumulative burden, actual ART transfers, and the seeded 300-graph ER/WS/BA ensemble. The script `reproduce_beijing_figure.py` regenerates the Beijing surveillance plot and annual descriptive totals from the supplied 192-month analysis CSV, retaining the missing December 2008 AIDS value as missing. The publication-styled versions of Figures 1 and 15 are regenerated by `Figure_Source/round2_figure_revisions.py`. The conceptual overview and synthesis diagrams are schematic rather than numerical outputs. The Supplementary Materials include the numerical result CSV files and the analysis copy of the monthly data.

For the nonlinear factorial comparisons we report three distinct resources: number of campaigns, total nominal campaign intensity $\sum_{n,k} P(k)u_{k,n}$, and actual mass $\sum_{n,k} P(k)u_{k,n}I_k(\tau_n^-)$ transferred from untreated to ART. Equal per-campaign intensity is not equivalent to an equal total resource budget when the event schedules differ. We therefore include an additional nominal-budget-matched periodic comparator in the nonlinear results section; this budget matching is not an assertion of equal monetary expenditure or equal ART uptake.

The synthetic graph ensemble evaluates structural thresholds and static row-susceptibility-removal proxies. It does not supply a compact-set common-weight certificate and does not reconstruct person-to-person contacts in Beijing. No biological selection of α or calibration of the treatment jump can be identified from aggregate case counts alone.

Choice and measurable diagnostics for the memory order.

The values $\alpha = 0.85$ and $\alpha = 1$ are prespecified illustrative orders, not epidemiologically estimated quantities. Two transparent within-model diagnostics are the absolute one-cycle spectral gain $g_\alpha(\Delta, U) = \rho[J(U)E_\alpha(\tau_c^{1-\alpha}A\Delta^\alpha)]$ and the dimensionless relative sensitivity $\mathcal{E}_\alpha = (\alpha/g_\alpha)\partial g_\alpha/\partial\alpha$ (estimated by central finite differences of the exact cycle-gain operator). Comparing $\alpha < 1$ with $\alpha = 1$ at matched rates, mixing and intervention parameters quantifies the role of memory in the defined hybrid mechanism; it *does not* justify 0.85 as the optimal observed order. Empirical identification would additionally require the original monthly case series, an observation equation connecting incidence to surveillance, comparable integer-order and fractional alternatives, and held-out prediction error or likelihood-based model selection (for example RMSE on a predeclared validation period). None of those fitted scores is reported without the primary observations and fitting program.

5.5. Explicit Common-Norm Certificate for a Finite Family

For a transparent constructive example, retain the uncorrelated 40-class mixing matrix and all parameters in (32) except set $\beta = 0.036$. Consider complete linkage $u_k = 1$ at every campaign, orders $\alpha \in \{0.85, 1\}$, and event intervals $\Delta \in \{1, 2, 3\}$ years. Define a single weight vector $w = (\mathbf{1}_{40}, 1000(1, 2, \ldots, 40))^\top \gg 0$ and the same weighted infinity norm for all six matrices. Direct complete-matrix multiplication (not an uncontrolled-flow eigenvalue proxy) gives

$$\max_{\substack{\alpha\in\{0.85,1\}\\ Delta\in\{1,2,3\}}} \max_{i=1,\ldots,80} \frac{[J(\mathbf{1})E_\alpha(A\Delta^\alpha)w]_i}{w_i} = 0.99800618 < q = 0.9981 < 1. \tag{35}$$

The factor $\tau_c^{1-\alpha} = 1$ numerically because $\tau_c = 1$ year. Since the six matrices are non-negative, Equation (35) certifies the same $\|\cdot\|_{w,\infty}$ for *any switching sequence* using these six admissible modes. The interval bound is $T_{\max} = 3$ years. This is a nontrivial constructive instance of Theorem 5, even though $\mathcal{R}_0 = 1.24345481 > 1$ for this modified example. Full instantaneous linkage is an idealized upper-effort scenario, not a practically established HIV policy. The result does *not* certify all $\alpha \in [0.85, 1]$, all $\Delta \in [1, 3]$, the original degree-pulse policy, or a changing ER/WS/BA topology. Table 3 lists the six mode-specific weighted-norm bounds used in the finite-family certificate.

Table 3. Common weighted-infinity-norm bounds for the six certified cycle matrices ($\beta = 0.036$, full linkage, and $w = (\mathbf{1}_{40}, 1000(1, 2, \ldots, 40))^\top$).

Fractional Order α	Interval Δ (Years)	Common-Norm Upper Bound
0.85	1	0.99799674
0.85	2	0.99682791
0.85	3	0.99661490
1.00	1	0.99800618
1.00	2	0.99637178
1.00	3	0.99595157

6. Numerical Results

6.1. Memory-Driven Transients, Trigger Activation, and Contraction Diagnostics

All new nonlinear results in this section use the 40 degree classes, the rates in Equation (32), and the source fractional model in Equation (4). The original nominal risk threshold $H_{up} = 0.003$ and refractory interval $h_r = 1$ year are kept in Section 5.2 as a historical nominal parameter statement. For the newly *declared active-trigger diagnostic* we instead use $H_{up} = 0.0018$, $h_r = 0.25$ years, and watchdog $T_{\max} = 2$ years. This alternative is necessary to produce nontrivial risk-trigger crossings over the 20-year synthetic horizon; it is not presented as a fitted intervention threshold. The renewed Caputo integrals are solved by the stated fractional PECE quadrature, $h = 0.05$ years unless otherwise noted. Endpoint crossings are assigned to the first eligible time-grid node. The watchdog always executes a campaign at the deadline and is included in event counts, nominal effort, and state jumps.

Figure 2 isolates the memory-order change in otherwise identical nonlinear interventions. All fractions are model-generated, not forecasts of observed HIV prevalence. Figure 3 shows actual event times, with triangle markers for both threshold-triggered and watchdog-forced interventions. The complete event log is exported by `reproduce_nonlinear_and_networks.py`.

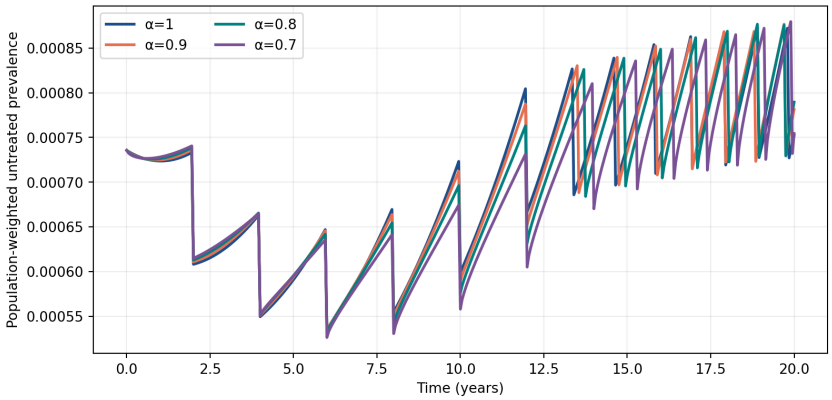


Figure 2. Newly computed nonlinear campaign-renewed Caputo simulations with $H_{up} = 0.0018$, $h_r = 0.25$ and watchdog $T_{\max} = 2$ years; all other epidemiological rates and degree-pulse intensities are held fixed. Time is in years and prevalence is population weighted.

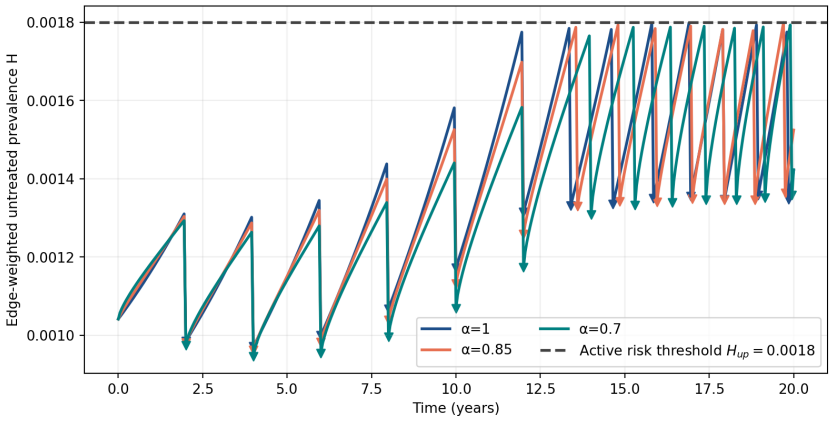


Figure 3. Edge-weighted untreated burden and realized risk/watchdog campaigns at fixed $H_{up} = 0.0018$, $h_r = 0.25$, $T_{\max} = 2$ years. Downward triangles mark actual intervention times. The horizontal dashed line marks the active risk-trigger threshold $H_{up} = 0.0018$; curve colors correspond to the fractional orders in the legend. Threshold crossings are quantized to the indicated numerical grid.

Figure 4 retains the independently verified exact 80×80 jump–flow matrix spectral gain. For the original $\beta = 0.09$ baseline, $\rho(G_{0.85}(U, 1)) = 1.06881753 > 1$; thus observed finite-horizon reductions cannot be relabeled as a uniform contraction certificate.

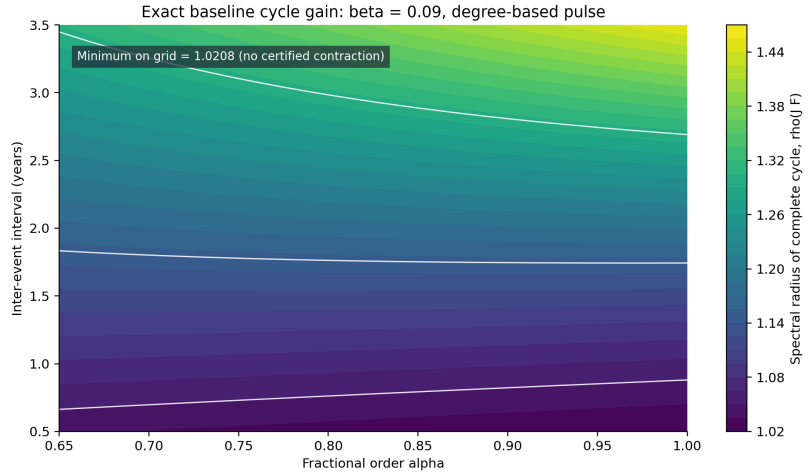


Figure 4. Independently reconstructed $\rho(J(U)E_\alpha(A\Delta^\alpha))$ for the stated supercritical baseline. The values exceed one in the shown range; no hybrid eradication certificate follows. Time is in years.

Figure 5 combines the actual nonlinear burden with the number of campaigns, directly exposing the cost of earlier triggering. The ranges of α and H_{up} are experimental sweeps, not estimated biological parameters.

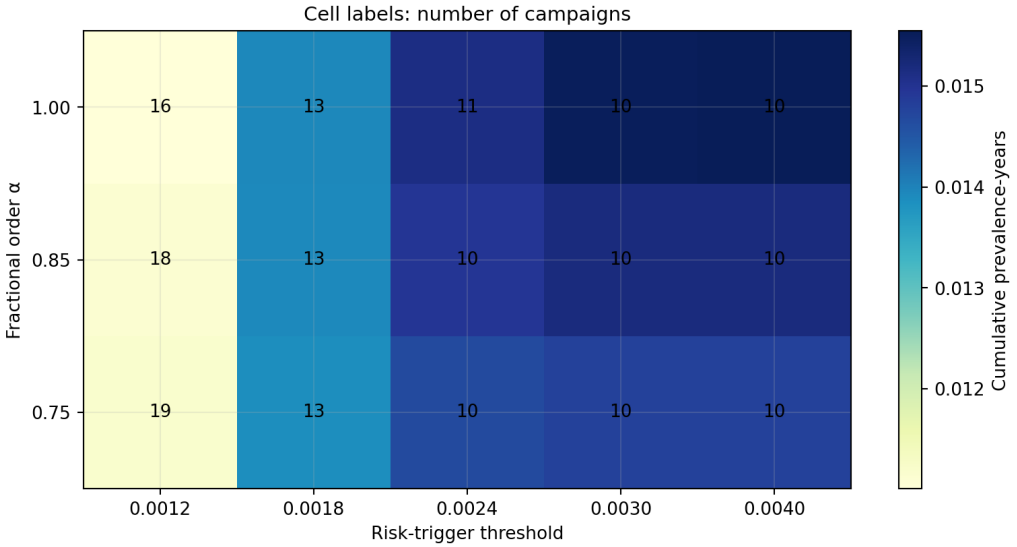


Figure 5. Nonlinear cumulative untreated burden in prevalence-years over memory-order and trigger-threshold scenarios. Each annotated cell reports the actual number of campaigns, including watchdog-triggered campaigns; all trajectories are newly integrated.

6.2. Control-Effort Trade-Offs, Robustness, and Cross-Network Performance

Figure 6 reconstructs the nonlinear burden–effort trade-off. We distinguish *nominal campaign effort* $E_{\mathrm{nom}} = \sum_n \sum_k P(k)u_{k,n}$ from the *actual population fraction transferred to ART*, $E_{\mathrm{ART}} = \sum_n \sum_k P(k)u_{k,n}I_k(\tau_n^-)$. These quantities are both output by the new program, are not interchangeable, and are not monetary treatment costs.

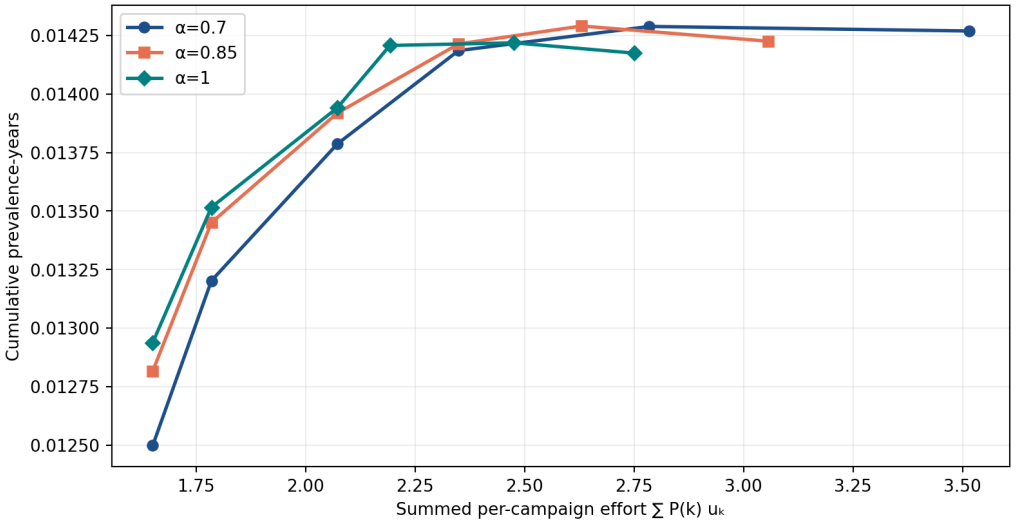


Figure 6. Numerically reconstructed burden–effort response, varying the maximum pulse size separately for three fractional orders; effort is the sum of population-weighted pulse fractions over actual campaigns (not the number of patients treated).

A second newly executable experiment samples 100 graphs from each of three canonical synthetic families (ER, WS and BA) with a fixed random seed. Each graph has 180 nodes. Actual graph degree distributions and mixing matrices are projected into

the class-level network threshold formula. Figure 7 displays the resulting threshold distributions; it does *not* verify Theorem 7's one-common-weight inequality under arbitrary switching and does not identify an observed Beijing HIV contact network. The graph instances, seeds, output thresholds and static comparator values are recorded individually in `synthetic_300_graph_ensemble.csv`.

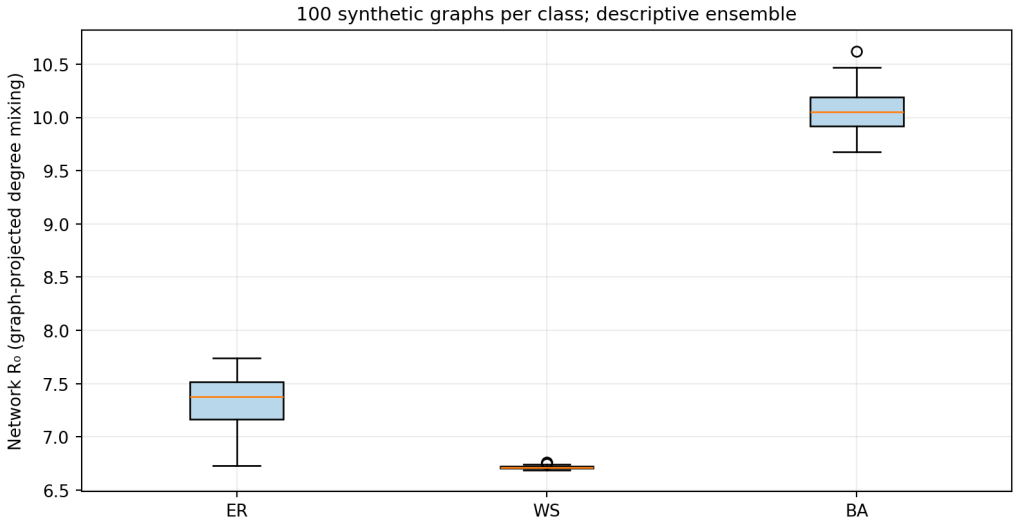


Figure 7. New synthetic ensemble: 100 seeded Erdős–Rényi, 100 Watts–Strogatz, and 100 Barabási–Albert networks ($N = 180$) summarized by graph-projected degree-mixing reproduction thresholds. Boxes show the interquartile range, center lines mark medians, whiskers extend to the most extreme observations within 1.5 interquartile ranges, and any points beyond the whiskers are outliers. No claim of real Beijing topology or a uniform switching-norm certificate is implied.

We also compute descriptive intervention-allocation proxies from the same graph matrices. The two proxy designs in Figures 8 and 9 remove a fixed share of susceptible-side contact intensity, either by degree or by local Perron row sensitivity. The equivalent nominal coverage is held fixed for both structural proxies. These are *static structural diagnostics*, not a claim that this graph experiment directly realizes the fractional pulse law of Proposition 2 or the common-norm requirement of Theorem 7.

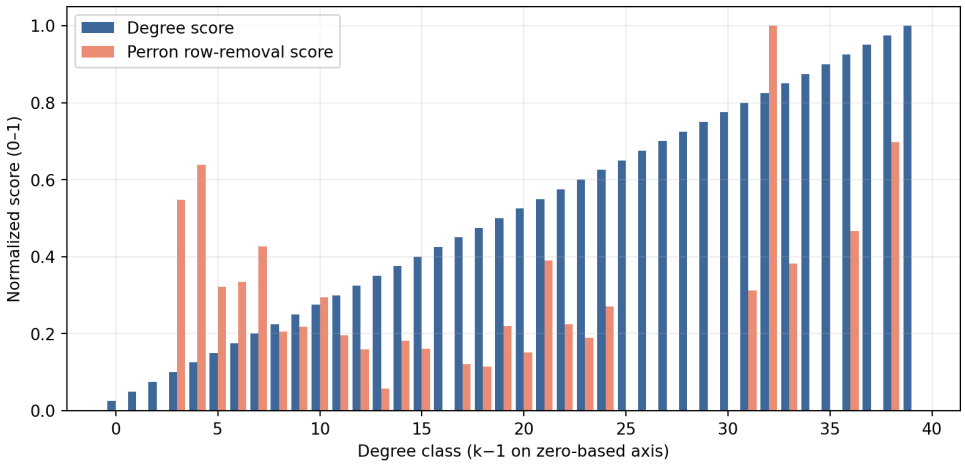


Figure 8. Degree score versus a Perron row-removal sensitivity proxy from the first of 100 newly generated BA graphs; these static structural scores are not an optimization of the complete fractional jump–flow operator.

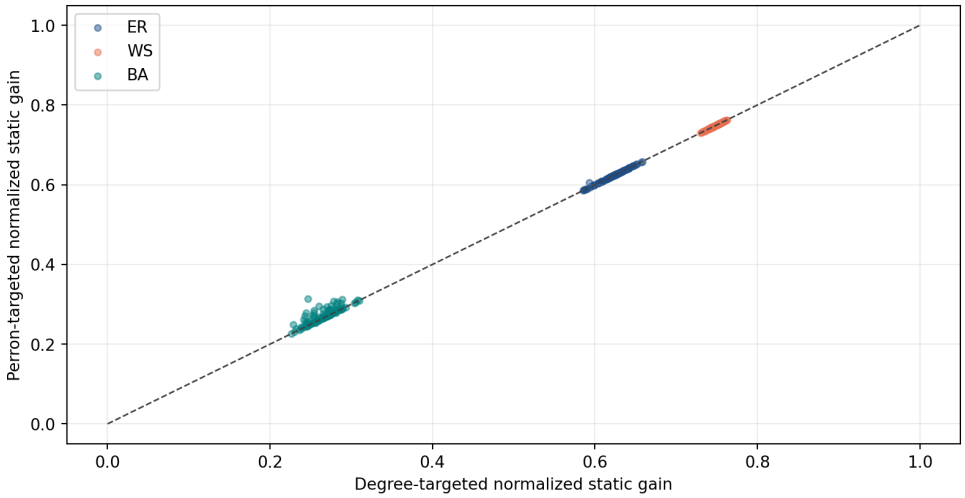


Figure 9. Degree versus Perron static structural intervention proxies, compared at the same approximate population-weighted coverage in 300 seeded synthetic networks; each dot is one graph. The dashed diagonal is the equality line between the two normalized scores. These proxies are separate from the treatment-jump theorem.

6.3. Numerical Reliability and Control-Parameter Diagnostics

With the nonlinear fractional PECE integrator and a fixed event-time grid, decreasing the time step from 0.10 to 0.05 to 0.025 years gives cumulative untreated prevalence-years 0.013897, 0.013919 and 0.013931, respectively, for the active-trigger $\alpha = 0.85$ case. All three computations have 13 campaigns, seven risk-triggered; small remaining differences reflect stepwise trigger localization and fractional product-integration error. This is a practical refinement check, not a mathematical global error bound.

Figure 10 checks time-step refinement under the same nonlinear event rule. Figure 11 distinguishes population-weighted untreated prevalence from the fraction receiving ART. Figure 12 varies only the upper intensity of the degree pulse, Figure 13 varies only the refractory interval, and Figure 14 varies threshold and intensity as a two-factor sensitivity study. All experiments apply both the threshold and the mandatory watchdog rules and report the resulting event counts.

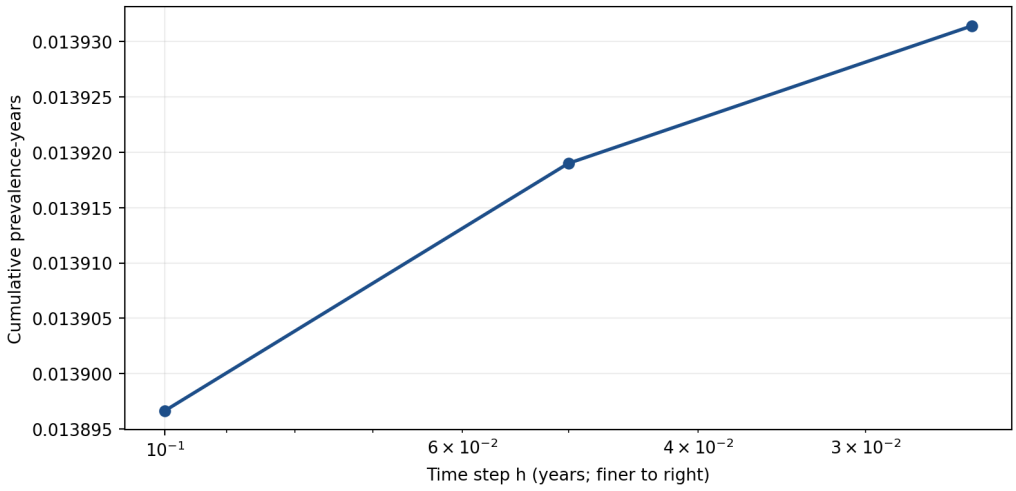


Figure 10. Adams–Bashforth–Moulton product-integration time-step refinement for the nonlinear risk-triggered scenario, including watchdog events. Event times are quantized to each grid; burden is in prevalence-years.

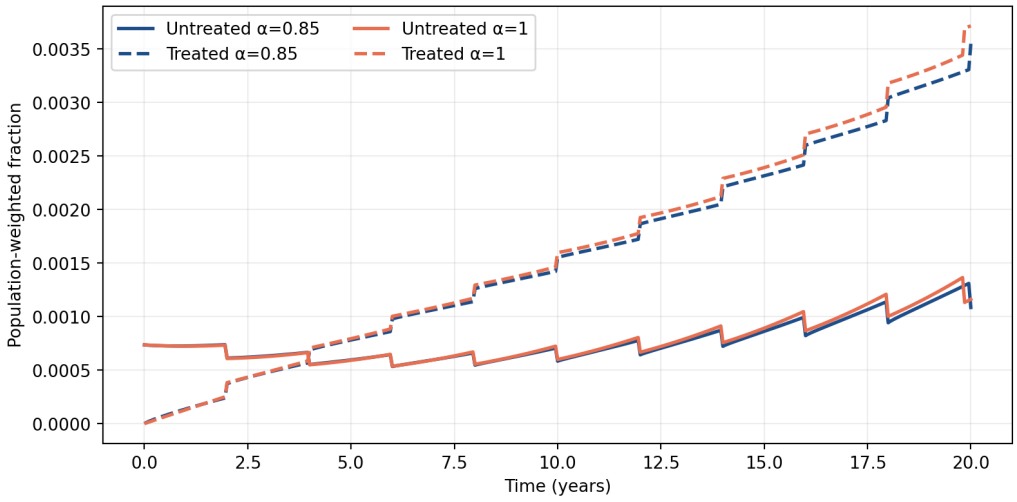


Figure 11. Recomputed untreated and treated population-weighted fractions in nonlinear fractional and integer-order campaign-renewed simulations under otherwise identical controls.

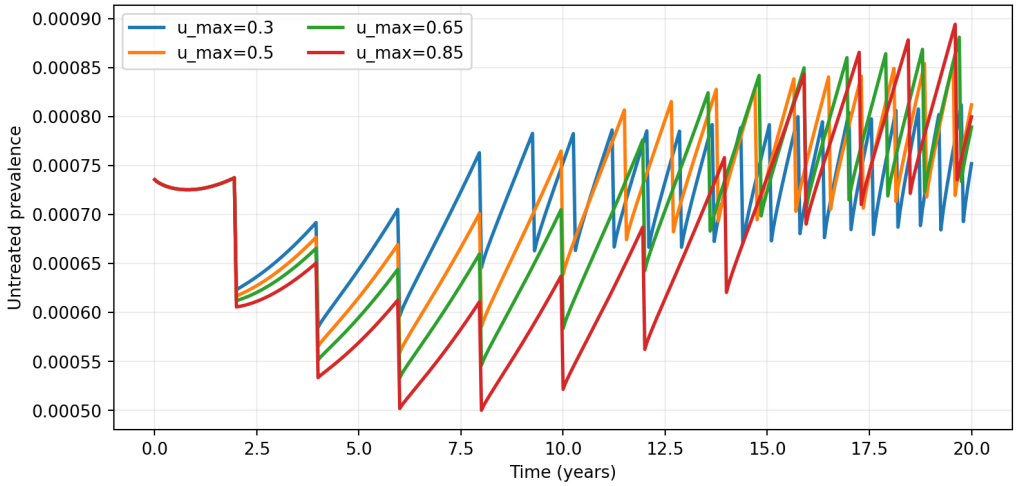


Figure 12. Sensitivity of nonlinear untreated prevalence to the admissible maximum treatment-linkage pulse, using the same event threshold, refractory interval and watchdog in each run.

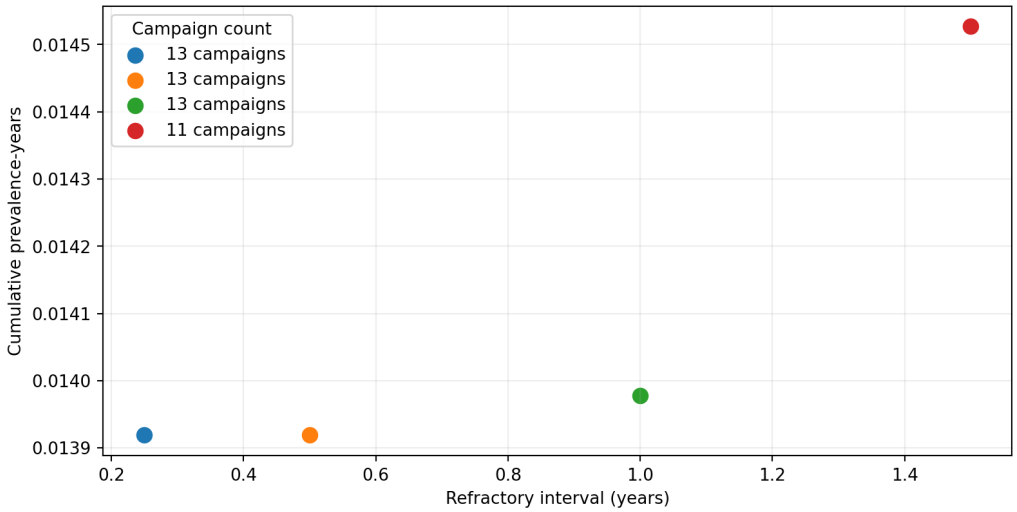


Figure 13. Nonlinear burden across refractory-interval choices with the same 2-year watchdog; markers distinguish actual numbers of campaigns.

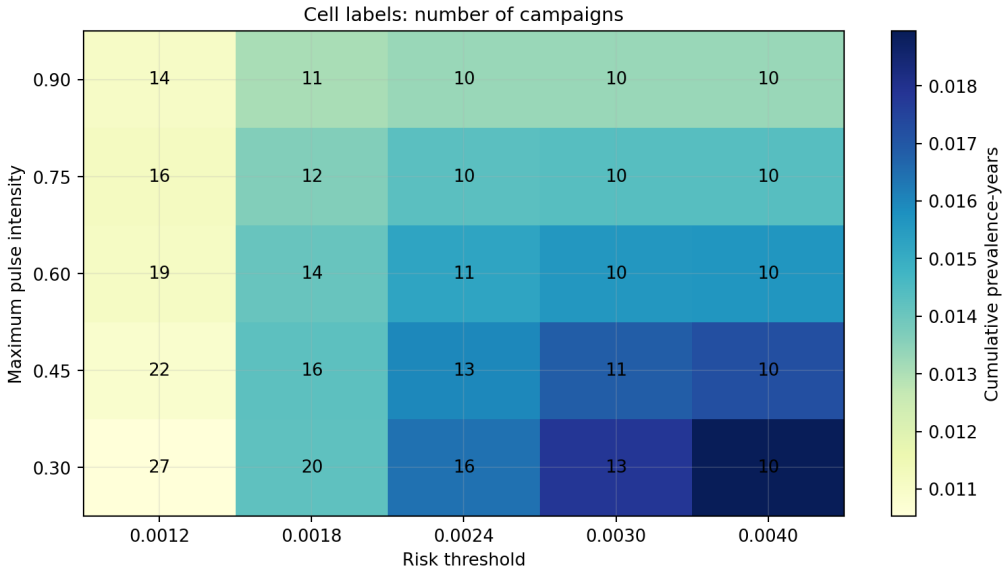


Figure 14. Nonlinear design map of cumulative untreated burden against trigger threshold and maximum pulse intensity. Cell labels give realized campaigns (risk- and watchdog-triggered).

Figure 15 remains the separate exact-matrix common-weight verification and must not be confused with the finite-time nonlinear outputs in Figures 10–14. In particular, the six-mode certificate uses $\beta = 0.036$ and idealized complete linkage $u_k = 1$, whereas the active-trigger simulation uses the original $\beta = 0.09$ and $u_{\max} = 0.65$.

6.4. Network Heterogeneity, Mixing, and Targeting Effectiveness

Figure 16 presents the synthetic-graph thresholds versus observed graph mean degree. Because the graph generators vary the distribution of edges as well as heterogeneity, the plot is only an ensemble description. For a controlled mixing perturbation, Figure 17 instead holds the 40-class degree distribution fixed while changing $C(r) = (1 - r)C_0 + rI$ for $r \in [0, 1]$. These scenarios are mathematical benchmarks, not empirical mobility or contact observations.

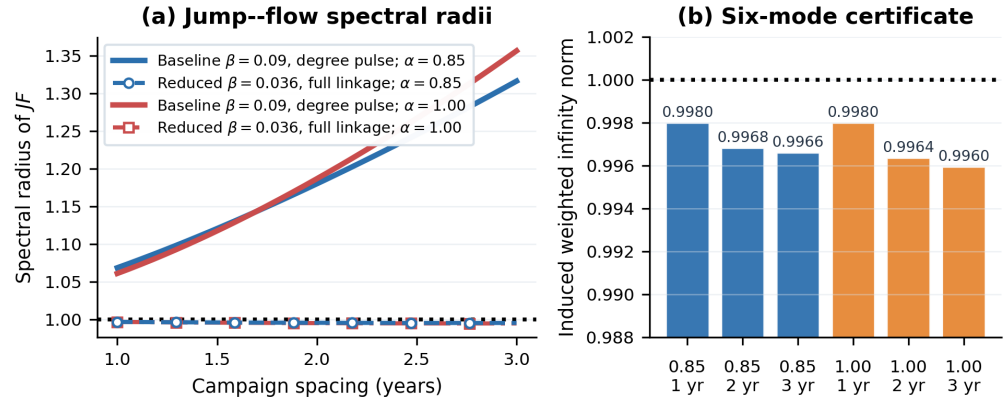


Figure 15. Audited complete-cycle spectral gains (**a**) and six-mode common weighted-infinity-norm bounds (**b**). The black dotted line marks the unit threshold in each panel. In panel (**a**), solid curves show the original $\beta = 0.09$ degree-pulse baseline; the reduced-$\beta = 0.036$ full-linkage curves are shown as a blue dashed line with open circles for $\alpha = 0.85$ and a red dash-dotted line with open squares for $\alpha = 1$. The blue dashed curve is present; the two reduced-parameter curves are close near unity, and the open markers distinguish them. In panel (**b**), each bar reports one of the six mode-specific bounds. A $\rho < 1$ for one matrix alone is not sufficient for arbitrary switching; the same weight is checked for every certified mode. Spacing is in years.

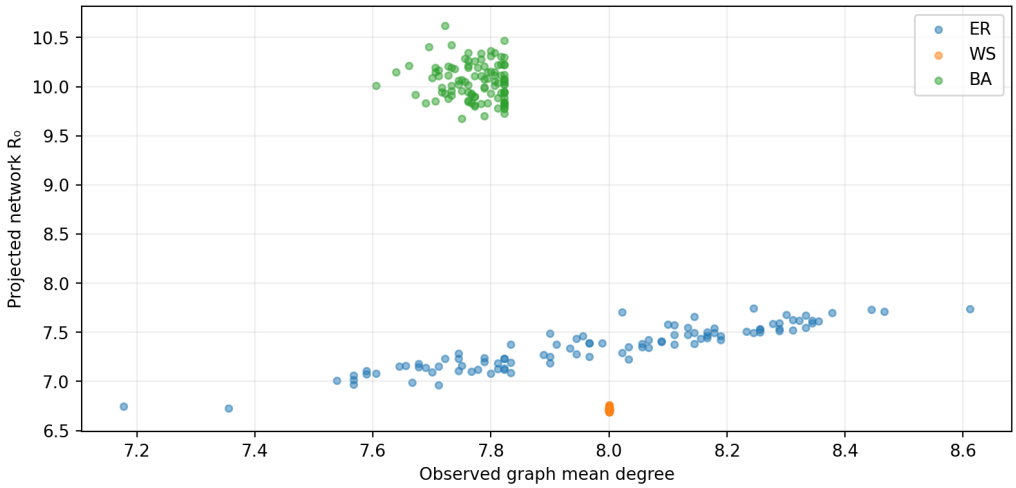


Figure 16. Graph-projected reproduction thresholds versus observed mean degree across 300 seeded ER/WS/BA synthetic graphs. The graph family differs in other properties; this panel is descriptive and not a one-factor causal identification.

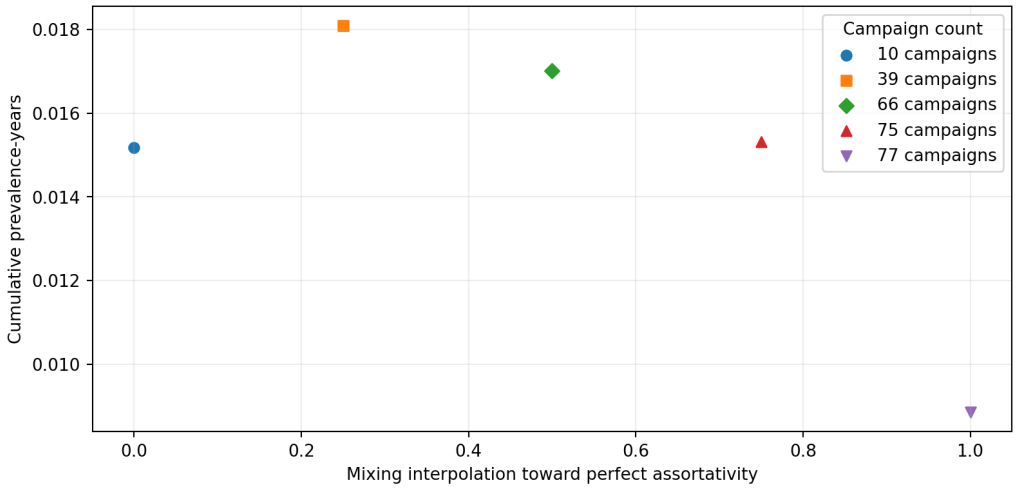


Figure 17. Nonlinear model comparison for a constructed family of mixing matrices $C(r) = (1 - r)C_0 + rI$; the underlying row-stochastic matrices interpolate from uncorrelated to perfectly assortative mixing. The event rule and degree law are fixed.

To address the editor's concern about comparisons changing several factors simultaneously, we report two distinct, explicitly labeled factorial experiments. The exact-cycle experiment in Table 4 holds the rates fixed and independently varies α, the *prescribed* interval, and class-targeted versus per-campaign mean-matched uniform linkage. All original baseline gains exceed one. These exact-matrix values do not themselves measure endogenous event times.

Figure 18 and Table 5 independently extend the comparison to nonlinear trajectories: order, fixed two-year periodic versus risk-triggered timing (with a two-year watchdog), and degree-targeted versus equal-per-campaign-mean uniform allocation are changed separately. A factor change can modify event frequency and hence lifetime nominal intervention effort, so a fixed-per-campaign comparison is not automatically an equal-total-budget comparison. The additional budget-matched periodic row increases its per-campaign degree pulse to match the risk policy's *total nominal* effort; all pulses remain within $[0, 1]$. Under this budget metric periodic control has *lower* simulated burden, so this paper does not claim universal superiority of event-triggered campaigns.

Table 4. Exact single-cycle spectral radii under separate memory-order, interval and pulse-allocation changes (baseline parameters). A per-campaign uniform pulse matches $\sum_k P(k)u_k = 0.15941257$. No entry below one is implied.

α	Interval (Years)	Uniform Pulse $\rho(G)$	Degree Pulse $\rho(G)$
1.00	1	1.08456508	1.06129604
1.00	3	1.44421032	1.35659817
0.85	1	1.09445717	1.06881753
0.85	3	1.39672345	1.31639903

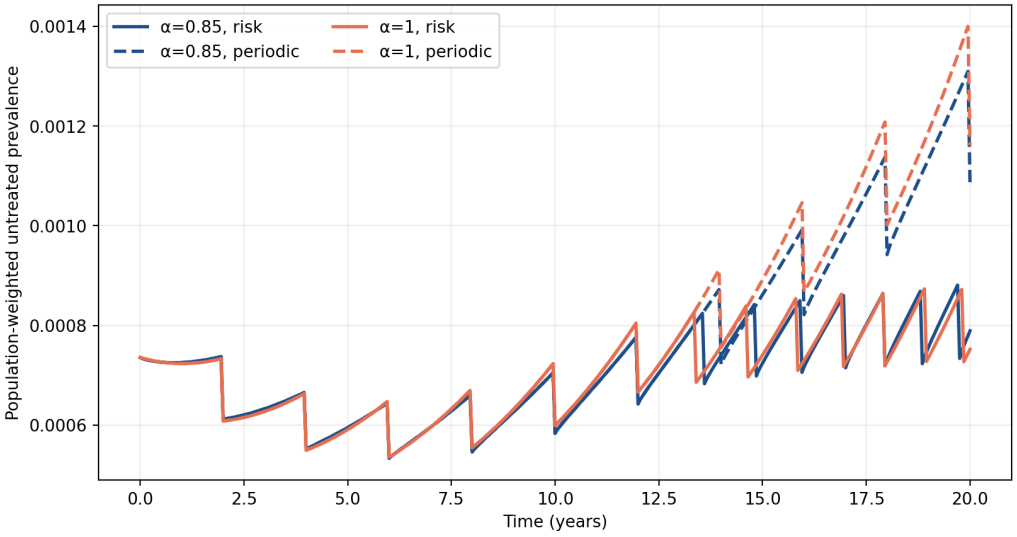


Figure 18. New nonlinear 20-year time-domain comparisons of risk-triggered versus two-year periodic interventions for $\alpha \in \{0.85, 1\}$ and the same degree-dependent pulse. All cases use common epidemiological parameters. The campaign counts and total effort differ and are reported explicitly in Table 5.

Table 5. New nonlinear 20-year control comparison, $h = 0.05$ years, $H_{up} = 0.0018$, $h_r = 0.25$ years, $T_{\max} = 2$ years. $E_{\text{nom}} = \sum_n \sum_k P(k)u_{k,n}$ is the nominal campaign effort; reported burden is prevalence-years.

α	Policy/Allocation	Campaigns	Risk Events	Burden	E_{nom}
0.85	Risk/degree	13	7	0.013919	2.07236
0.85	Periodic/degree	10	0	0.015185	1.59413
0.85	Periodic/degree (budget matched)	10	0	0.011803	2.07236
0.85	Risk/uniform	25	22	0.013744	3.98531
1.00	Risk/degree	13	7	0.013942	2.07236
1.00	Periodic/degree	10	0	0.015546	1.59413
1.00	Periodic/degree (budget matched)	10	0	0.012022	2.07236
1.00	Risk/uniform	21	18	0.013678	3.34766

6.5. Sensitivity Priorities and Integrated Design Synthesis

Figure 19 separately reports dimensionless local elasticities of the exact linear-cycle spectral radius, computed with ±1% perturbations and fixed physical units. It provides a well-defined within-model sensitivity index, not an estimate of the fractional order from reported monthly incidence. Figure 20 retains the original conceptual synthesis of the model's two connected design layers.

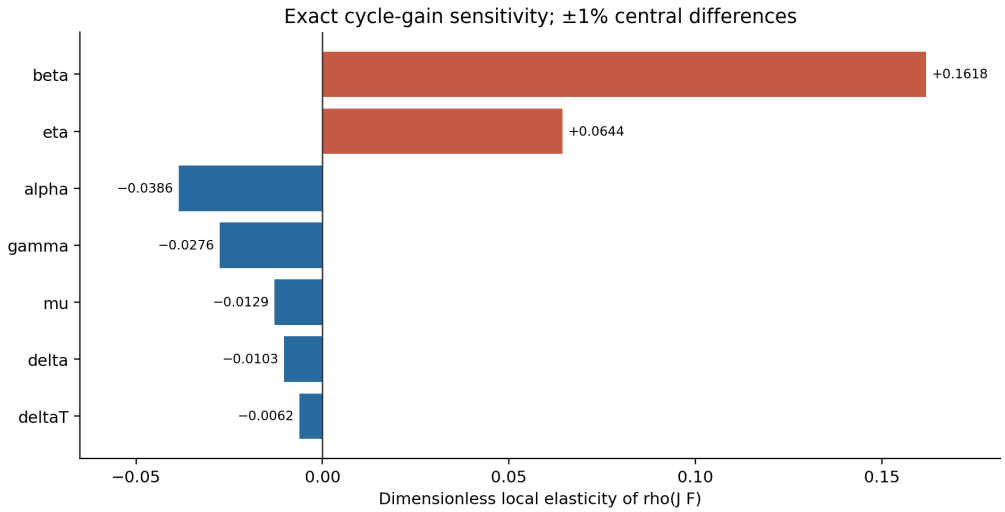


Figure 19. Normalized local elasticities of the exact cycle spectral radius, approximated by central ±1% perturbations of each parameter, $\alpha = 0.85$, $\Delta = 1$ year, and the original degree-targeted pulse. Positive values increase cycle gain; negative values decrease it. Negative values use a true minus sign, and the labels are placed outside the bars to avoid overlap.

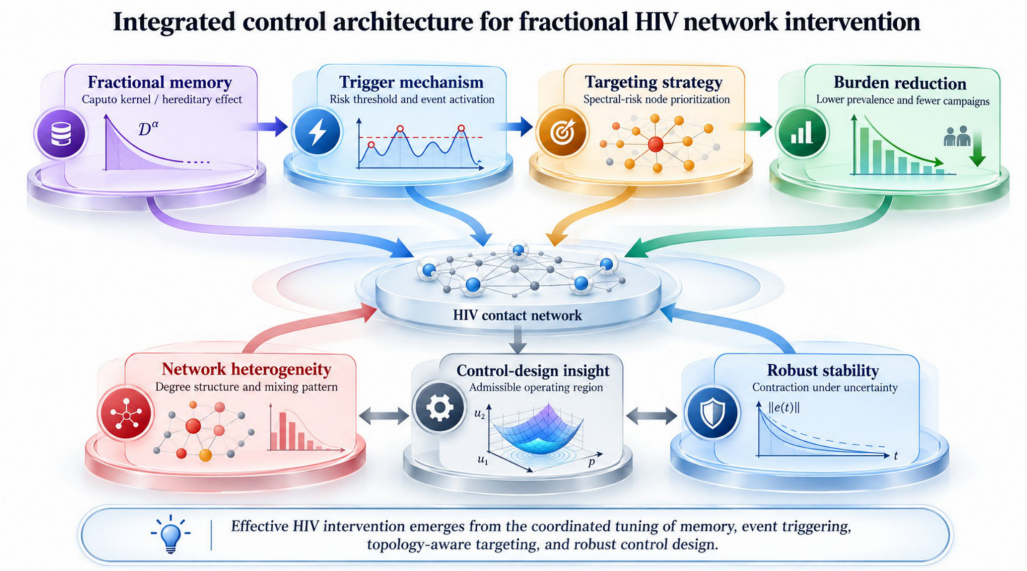


Figure 20. Integrated schematic summary of the numerical mechanism and control-design implications. The color-coded modules denote fractional memory (purple), triggering (blue), spectral-risk targeting (orange), burden reduction (green), network heterogeneity (red), control-design insight (gray), and robust stability (blue). Solid colored arrows show conceptual dependencies linking these modules to the HIV contact network; gray double-headed arrows indicate iterative feedback between network heterogeneity, control design, and robust stability. The curves, bars, node diagrams, and response surfaces are schematic icons, not quantitative plots or measured causal effects.

6.6. Memory-Convention Sensitivity and Empirical Surveillance Context

Figure 21 is regenerated from the new solver for the same synthetic risk-trigger parameter set. The renewed-memory solution restarts the Caputo fractional integral at each campaign. The second curve instead uses an explicitly stated fixed-history *impulsive Volterra integral convention*: the continuous history kernel retains all prior nonlinear right-hand-side evaluations, while discrete ART jumps enter additively in the integral representation. These are different hybrid models; the comparison is finite-horizon sensitivity analysis only, and does not transfer Theorems 5–7 to a full-history Caputo system without a new proof.

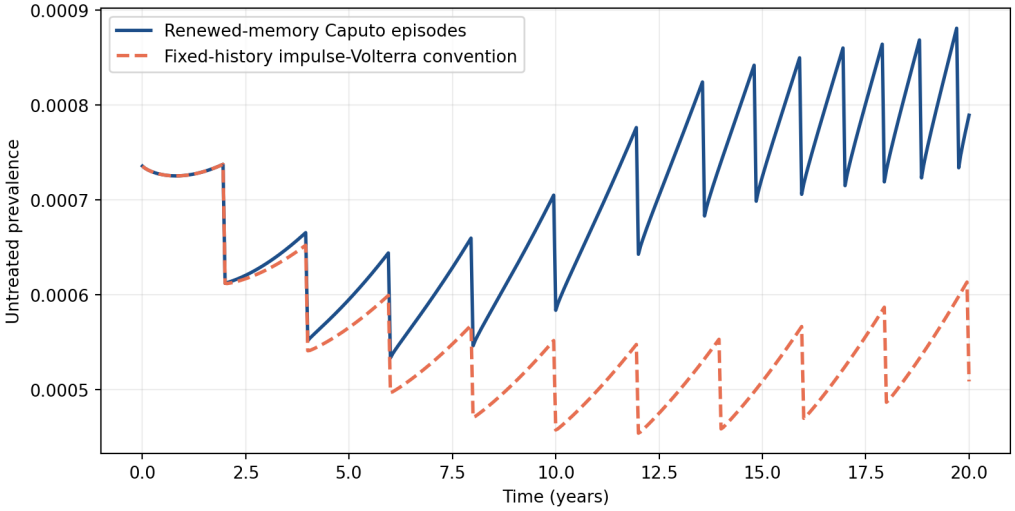


Figure 21. Newly computed numerical comparison between renewed-memory Caputo episodes and a precisely defined fixed-history impulsive Volterra integral convention, using identical rates and threshold inputs. The conventions are mathematically distinct; no full-history stability theorem is inferred.

The authors' previously provided Beijing data file, *Beijing 2005–2020 HIV/AIDS monthly statistics*, contains 192 records, January 2005 through December 2020, and separate monthly reported HIV and AIDS cases and rates. We have retrieved the original CSV and reconstructed Figure 22 and a source-derived annual totals CSV. The HIV reported-case column is complete over the 192 dates. The AIDS reported-case column has *one missing observation*: December 2008 is marked "–" in the source. The missing value is neither imputed nor treated as zero; the 2008 AIDS annual sum therefore represents only the 11 observed months. No population normalization or causal reconstruction of infection times is attempted.

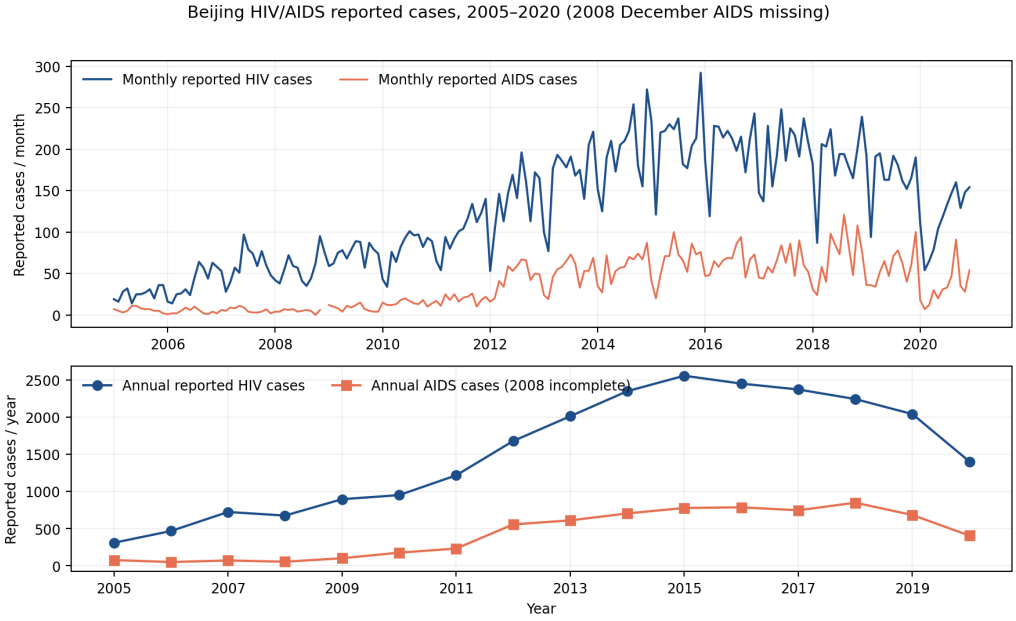


Figure 22. Beijing monthly HIV and AIDS reported-case counts and calendar-year descriptive totals (January 2005–December 2020), regenerated from the 192-row source CSV. December 2008 AIDS counts are coded as missing (not zero or interpolated), so the 2008 AIDS annual sum is incomplete. These surveillance counts are not fitted prevalence trajectories or network-control validation.

The observed count series is descriptive reporting context, not a measurement of the latent degree-class prevalence variables in the nonlinear model. Without a defensible observation operator, ascertainment model and matching contact-network measurements, this series cannot identify the fractional memory order, fit the event rule, or validate the synthetic network targeting policy. In particular, no RMSE, likelihood or out-of-sample predictive skill for this HIV control framework is claimed. The CSV, missing-data audit, annual aggregations and plotting code are included in the reproducibility Supplement.

7. Discussion

The principal control-theoretic result is conditional, rather than an unrestricted eradication assertion. For the campaign-renewed Caputo formulation, a positive Mittag–Leffler inter-event matrix followed by a non-negative treatment jump yields a complete-cycle operator. Uniform decay of the repeatedly renewed hybrid trajectory follows when every admissible cycle contracts in one common monotone norm and the watchdog ensures a finite upper bound on campaign spacing. The resulting physical-time exponential envelope is a consequence of repeatedly multiplying strictly contractive *cycles*; it is not the decay law of one uninterrupted fractional system. This distinction prevents the stability claim from being transferred to full-history Caputo dynamics without a new analysis.

The mathematical comparison issue is equally substantive. Untreated infection dynamics include susceptible depletion, and the nonlinear infected–treated subsystem need not be cooperative. The corrected proofs instead use a non-negative forcing residual and the positive resolvent of the disease-free Metzler comparison matrix. This supports an interval-wise upper comparison and, under the common cycle norm, nonlinear extinction for the explicitly renewed-memory system. It does not require non-negative off-diagonal derivatives of the original nonlinear infected subsystem.

The complete-matrix audit illustrates why these conditions matter. With the stated baseline, $\mathcal{R}_0 = 3.10863703$ and the degree-pulse cycle at $\alpha = 0.85$, $\Delta = 1$ year has spectral radius 1.06881753; therefore this setting cannot be labeled contractive. Under an explicitly different and idealized parameter policy ($\beta = 0.036$, $u_k = 1$), the finite six-mode family possesses a single common weight with maximum induced gain 0.99800618. This example establishes feasibility for exactly the declared admissible modes, not a uniform margin over continuous memory-order, network-topology or event-time uncertainty. In particular, the historical ER/WS/BA ensemble panels are not proof of Theorem 7. The new nonlinear factorial study isolates fractional order, intervention timing and class allocation under explicitly stated experimental controls. Risk-triggered interventions reduce the burden relative to fixed-periodic interventions at equal per-campaign pulse intensity in one synthetic scenario, but cause more campaigns and consume higher nominal total effort. When total nominal effort is matched, the periodic degree-targeted strategy achieves a smaller simulated burden in this example. The numerical evidence therefore does not establish universal superiority of triggering.

Operationally, the memory reset is best understood as a reduced-memory surveillance approximation in which the effective observation episode begins anew after screening/linkage. This may be reasonable in a cohort or data-system with limited retained pre-campaign history, but it is not a biological mechanism for eliminating past infection or behavioral exposure. The newly regenerated Figure 21 illustrates the difference between the restarted Caputo and fixed-history impulsive Volterra conventions without validating the restart approximation biologically. An analogous boundary arises in network interpretation: the model has $3K$ living state variables and K cumulative-mortality accounts, but its degree closure is not a measured individual contact graph, and it does not resolve all HIV clinical stages.

Finally, the Beijing surveillance panel (Figure 22) is descriptive context only. Without longitudinal treatment events, contact topology, an observation model, and adequate primary data, one cannot identify the fractional order, estimate targeting effects, or validate intervention timing. The revised supplement now includes reproducible fractional nonlinear simulations, 300 seeded synthetic graph realizations and the recovered 192-month Beijing count series. Figure 22 marks the missing December 2008 AIDS value without imputation. The empirical records still cannot identify the contact graph, fractional order or counterfactual treatment effect. A meaningful next step is a model-comparison exercise against integer-order alternatives with matched state resolution and held-out outcomes, followed by a clinical-state extension for which the positive comparison and common-weight assumptions can be proved.

8. Conclusions

This paper develops a fractional-order event-triggered control framework for HIV transmission on heterogeneous contact networks and positions fractional dynamics at the center of the control problem. The model combines Caputo memory, network-based infection pressure, degree-targeted intervention, and campaign-triggered jumps within a unified mathematical setting. On the analytical side, the study establishes positivity and biological invariance, derives the network spectral threshold, and proves local threshold stability together with sufficient global eradication conditions through a fractional jump–flow contraction argument.

The control contribution is twofold. First, a robust hybrid stability criterion is derived under uncertainty in memory order, topology, parameters, and trigger timing, showing that contraction of the repeated jump–flow operator provides a verifiable route to eradication. Second, a Perron-sensitivity intervention score is obtained, yielding a topology-aware targeting rule that generalizes purely degree-based control. These results show that fractional memory is not an isolated modeling embellishment; it interacts directly with when interventions are activated and where finite resources should be deployed.

The numerical diagnostics distinguish a noncontractive baseline from a separate, idealized six-mode control family that satisfies one common weighted-norm certificate. The original baseline therefore does not automatically guarantee eradication. Together with the memory-convention sensitivity experiment and the Beijing surveillance context, these results show that effective HIV intervention on complex networks emerges from the joint tuning of hereditary dynamics, event triggering, network structure, and finite-resource targeting. Future work should estimate memory parameters from longitudinal data, replace synthetic network closures with empirically resolved contact or mobility structure, and extend the present theory to noninstantaneous and full-history impulsive interventions.

Supplementary Materials: The following supporting information can be downloaded at: https://www.mdpi.com/article/10.3390/fractalfract10110762/s1. The reproducibility ZIP contains Supplementary Code S1: `reproducible_cycle_audit.py`, `reproduce_nonlinear_and_networks.py`, and `reproduce_beijing_figure.py`; the publication-styled Figures 1 and 15 regeneration script `round2_figure_revisions.py`; the 192-row January 2005–December 2020 Beijing monthly HIV/AIDS analysis CSV (Supplementary Data S1); and machine-readable numerical audit, convergence, trigger-grid, memory-convention, and 300-graph ensemble outputs. The scripts were run with Python 3.13.5, NumPy 2.3.5, SciPy 1.17.0, Matplotlib 3.10.8, NetworkX 3.6.1, and pandas 2.2.3. The Beijing data are aggregate reported counts; the missing December 2008 AIDS value is retained as missing.

Author Contributions: Conceptualization, T.D., H.W. and Y.Z.; methodology, T.D., H.W. and Y.Z.; software, T.D.; formal analysis, T.D., H.W. and Y.Z.; investigation, T.D.; data curation, T.D.; writing—original draft preparation, T.D.; writing—review and editing, H.W., Y.Z., Q.W. and S.W.;

visualization, T.D.; supervision, H.W., Y.Z. and S.W.; project administration, T.D.; funding acquisition, T.D. All authors have read and agreed to the published version of the manuscript.

Funding: This research was funded by the Yunnan Provincial Universities Joint Special Project—General Program (grant number 202501BA070001-104), awarded to Tingting Dai at Zhaotong University. Shaohui Wang acknowledges support from the Board of Regents Carolyn Adams Dawson Professorship (no grant number).

Institutional Review Board Statement: Not applicable. The empirical component uses only aggregate, publicly accessible surveillance statistics and does not involve identifiable individual-level human-participant data.

Informed Consent Statement: Not applicable.

Data Availability Statement: The supplied source CSV for Beijing HIV/AIDS case reports, January 2005–December 2020, consists of 192 dated monthly rows and is credited to the Public Health Science Data Center of the Chinese CDC [40]; the supplement provides the analysis copy and a field-level missingness audit. December 2008 AIDS case counts are missing in that source and are neither treated as zero nor imputed. Source code and machine-readable outputs are provided for the newly implemented fractional nonlinear event-triggered model, 300 seeded synthetic graph realizations, and exact 80-dimensional cycle-matrix computations. The original conceptual diagrams do not correspond to numeric data. No individual HIV contact graph or patient-level treatment history is available; the Beijing count series is not a fitted validation of the controller. Redistribution of the source surveillance copy remains subject to verification of the originating data provider's applicable terms; if required, the authors will provide the official source link and derived aggregate outputs instead of redistributing the original CSV.

Acknowledgments: During the preparation of this manuscript, the authors used OpenAI ChatGPT (GPT-6) and OpenAI image-generation tools for language editing, LaTeX-formatting assistance, and graphical-layout refinement. The authors reviewed and edited all outputs and take full responsibility for the content of the publication.

Conflicts of Interest: The authors declare no conflicts of interest. The funder had no role in the design of the study; in the collection, analysis, or interpretation of data; in the writing of the manuscript; or in the decision to publish the results.

References

1. Pastor-Satorras, R.; Vespignani, A. Epidemic spreading in scale-free networks. *Phys. Rev. Lett.* **2001**, *86*, 3200–3203. [CrossRef] [PubMed]
2. Pastor-Satorras, R.; Castellano, C.; Van Mieghem, P.; Vespignani, A. Epidemic processes in complex networks. *Rev. Mod. Phys.* **2015**, *87*, 925–979. [CrossRef]
3. Newman, M.E.J. Assortative mixing in networks. *Phys. Rev. Lett.* **2002**, *89*, 208701. [CrossRef] [PubMed]
4. Castellano, C.; Pastor-Satorras, R. Thresholds for epidemic spreading in networks. *Phys. Rev. Lett.* **2010**, *105*, 218701. [CrossRef] [PubMed]
5. Cohen, R.; Havlin, S.; ben-Avraham, D. Efficient immunization strategies for computer networks and populations. *Phys. Rev. Lett.* **2003**, *91*, 247901. [CrossRef] [PubMed]
6. Pastor-Satorras, R.; Vespignani, A. Immunization of complex networks. *Phys. Rev. E* **2002**, *65*, 036104. [CrossRef] [PubMed]
7. Van Mieghem, P.; Omic, J.; Kooij, R. Virus spread in networks. *IEEE/ACM Trans. Netw.* **2009**, *17*, 1–14. [CrossRef]
8. Masuda, N. Immunization of networks with community structure. *New J. Phys.* **2009**, *11*, 123018. [CrossRef]
9. Cohen, M.S.; Chen, Y.Q.; McCauley, M.; Gamble, T.; Hosseinipour, M.C.; Kumarasamy, N.; Hakim, J.G.; Kumwenda, J.; Grinsztejn, B.; Pilotto, J.H.S.; et al. Antiretroviral therapy for the prevention of HIV-1 transmission. *N. Engl. J. Med.* **2016**, *375*, 830–839. [CrossRef] [PubMed]
10. Rodger, A.J.; Cambiano, V.; Bruun, T.; Vernazza, P.; Collins, S.; van Lunzen, J.; Corbelli, G.M.; Estrada, V.; Geretti, A.M.; Beloukas, A.; et al. Risk of HIV transmission through condomless sex in serodifferent gay couples with suppressive ART: The PARTNER2 study. *Lancet* **2019**, *393*, 2428–2438. [CrossRef] [PubMed]
11. Grant, R.M.; Lama, J.R.; Anderson, P.L.; McMahan, V.; Liu, A.Y.; Vargas, L.; Goicochea, P.; Casapía, M.; Guanira-Carranza, J.V.; Ramirez-Cardich, M.E.; et al. Preexposure chemoprophylaxis for HIV prevention in men who have sex with men. *N. Engl. J. Med.* **2010**, *363*, 2587–2599. [CrossRef] [PubMed]

12. Podlubny, I. *Fractional Differential Equations*; Academic Press: San Diego, CA, USA, 1999; ISBN 978-0-12-558840-9.
13. Kilbas, A.A.; Srivastava, H.M.; Trujillo, J.J. *Theory and Applications of Fractional Differential Equations*; Elsevier: Amsterdam, The Netherlands, 2006; ISBN 978-0-444-51832-3.
14. Diethelm, K. *The Analysis of Fractional Differential Equations*; Springer: Berlin/Heidelberg, Germany, 2010. [CrossRef]
15. Matignon, D. Stability results for fractional differential equations with applications to control processing. In *Computational Engineering in Systems Applications*; IMACS/IEEE-SMC: Lille, France, 1996; Volume 2, pp. 963–968.
16. Li, Y.; Chen, Y.Q.; Podlubny, I. Mittag–Leffler stability of fractional order nonlinear dynamic systems. *Automatica* **2009**, *45*, 1965–1969. [CrossRef]
17. Almoneef, A.A.; Barakat, M.A.; Hyder, A.-A. Analysis of the fractional HIV model under proportional Hadamard–Caputo operators. *Fractal Fract*. **2023**, *7*, 220. [CrossRef]
18. Ullah, S.; Altanji, M.; Khan, M.A.; Alshaheri, A.; Sumelka, W. The dynamics of HIV/AIDS model with fractal-fractional Caputo derivative. *Fractals* **2023**, *31*, 2340015. [CrossRef]
19. Li, J.; Yu, Y.; Lu, Z.; Xu, W. Stability of a fractional HIV/AIDS epidemic model with drug control by continuous-time random walk. *Fractal Fract*. **2026**, *10*, 248. [CrossRef]
20. Heemels, W.P.M.H.; Johansson, K.H.; Tabuada, P. An introduction to event-triggered and self-triggered control. In Proceedings of the 51st IEEE Conference on Decision and Control, Maui, HI, USA, 10–13 December 2012; pp. 3270–3285. [CrossRef]
21. Postoyan, R.; Tabuada, P.; Nešić, D.; Anta, A. A framework for the event-triggered stabilization of nonlinear systems. *IEEE Trans. Autom. Control* **2015**, *60*, 982–996. [CrossRef]
22. Li, X.; Yang, X.; Cao, J. Event-triggered impulsive control for nonlinear delay systems. *Automatica* **2020**, *117*, 108981. [CrossRef]
23. Goebel, R.; Sanfelice, R.G.; Teel, A.R. *Hybrid Dynamical Systems: Modeling, Stability, and Robustness*; Princeton University Press: Princeton, NJ, USA, 2012. [CrossRef]
24. Li, X.; Peng, D.; Cao, J. Lyapunov stability for impulsive systems via event-triggered impulsive control. *IEEE Trans. Autom. Control* **2020**, *65*, 4908–4913. [CrossRef]
25. Peng, D.; Li, X.; Rakkiyappan, R.; Ding, Y. Stabilization of stochastic delayed systems: Event-triggered impulsive control. *Appl. Math. Comput*. **2021**, *401*, 126054. [CrossRef]
26. Xu, J.; Liu, Y.; Qiu, J.; Lu, J. Event-triggered impulsive control for nonlinear stochastic delayed systems and complex networks. *Commun. Nonlinear Sci. Numer. Simul*. **2025**, *140*, 108305. [CrossRef]
27. Sun, Y.; Lu, J.; Xing, M.; Ruan, Q.; Lou, J. Event-triggered impulsive stabilization of nonlinear delayed systems with application to network synchronization. *Commun. Nonlinear Sci. Numer. Simul*. **2026**, *159*, 109862. [CrossRef]
28. Li, M. Data-driven event-triggered scheme for model-unknown fractional-order networked control systems: A parametrization transform method. *Fractal Fract*. **2026**, *10*, 345. [CrossRef]
29. Sun, J.; Zhou, J.; Zhang, Y.; Zhou, X.; Zhang, S. Event-triggered quantized synchronization via sampled-data iterative learning control for coupled fractional-order time-delayed competitive neural networks. *Fractal Fract*. **2026**, *10*, 606. [CrossRef]
30. Zheng, H.; Zhang, C.; Xu, Y.; Yan, P.; Shi, Z.; Zhang, G. Fully distributed dynamic event-triggered observer-based H_∞ consensus control of fractional-order multi-agent systems. *Fractal Fract*. **2026**, *10*, 624. [CrossRef]
31. Zhang, C.; Shen, H.; Ma, L.; Shi, Z.; Zhang, G. Dynamic event-triggered fixed-time practical distributed optimization and output consensus of incommensurate nonlinear fractional-order multi-agent systems with input saturation. *Fractal Fract*. **2026**, *10*, 591. [CrossRef]
32. Liu, N.; Wang, J.; Lan, Q.; Deng, W. Dynamics and event-triggered impulsive control of a fractional-order epidemic model with time delay. *Fractal Fract*. **2024**, *8*, 22. [CrossRef]
33. Liu, N.; Fang, J.; Sun, J.; Li, S. Epidemic dynamics of a fractional-order SIR weighted network model and its targeted immunity control. *Fractal Fract*. **2022**, *6*, 232. [CrossRef]
34. Gokul, P.; Kashkynbayev, A.; Prakash, M.; Rajan, R. Finite-time contractive stabilization for fractional-order switched systems via event-triggered impulse control. *Commun. Nonlinear Sci. Numer. Simul*. **2025**, *143*, 108658. [CrossRef]
35. Diekmann, O.; Heesterbeek, J.A.P.; Metz, J.A.J. On the definition and the computation of the basic reproduction ratio in models for infectious diseases in heterogeneous populations. *J. Math. Biol*. **1990**, *28*, 365–382. [CrossRef] [PubMed]
36. van den Driessche, P.; Watmough, J. Reproduction numbers and sub-threshold endemic equilibria for compartmental models of disease transmission. *Math. Biosci*. **2002**, *180*, 29–48. [CrossRef] [PubMed]
37. Berman, A.; Plemmons, R.J. *Nonnegative Matrices in the Mathematical Sciences*; SIAM: Philadelphia, PA, USA, 1994. [CrossRef]
38. Diethelm, K.; Ford, N.J.; Freed, A.D. A predictor–corrector approach for the numerical solution of fractional differential equations. *Nonlinear Dyn*. **2002**, *29*, 3–22. [CrossRef]

39. Garrappa, R. Numerical solution of fractional differential equations: A survey and a software tutorial. *Mathematics* **2018**, *6*, 16. [CrossRef]
40. Public Health Science Data Center, Chinese Center for Disease Control and Prevention. HIV/AIDS Infectious-Disease Surveillance Data Query: Beijing Monthly Reports, 2005–2020. Available online at the Official Public Health Science Data Center HIV/AIDS Database. Available online: https://www.phsciencedata.cn/Share/ky_sjml.jsp?id=c2ca694e-3995-4c7f-9078-3ed0aaf14556 (accessed on 23 October 2026).

Disclaimer/Publisher's Note: The statements, opinions and data contained in all publications are solely those of the individual author(s) and contributor(s) and not of MDPI and/or the editor(s). MDPI and/or the editor(s) disclaim responsibility for any injury to people or property resulting from any ideas, methods, instructions or products referred to in the content.